



# A Novel Metal-Based Imaging Probe for Targeted Dual-Modality SPECT/MR Imaging of Angiogenesis

Charalampos Tsoukalas<sup>1</sup>, Dimitrios Psimadas<sup>1</sup>, George A. Kastis<sup>1,2</sup>, Vassilis Koutoulidis<sup>3</sup>, Adrian L. Harris<sup>4</sup>, Maria Paravatou-Petsotas<sup>1</sup>, Maria Karageorgou<sup>1,5</sup>, Lars R. Furenlid<sup>6,7</sup>, Lia A. Mouloupoulos<sup>3</sup>, Dimosthenis Stamopoulos<sup>5,8</sup> and Penelope Bouziotis<sup>1\*</sup>

## OPEN ACCESS

### Edited by:

Lorenzo Tei,  
Università degli Studi del Piemonte  
Orientale, Italy

### Reviewed by:

Graeme J. Stasiuk,  
University of Hull, United Kingdom  
Johannes Notni,  
Technische Universität München,  
Germany  
Calogero D'Alessandria,  
Klinikum rechts der Isar, Technische  
Universität München, Germany

### \*Correspondence:

Penelope Bouziotis  
bouzioti@rrp.demokritos.gr

### Specialty section:

This article was submitted to  
Medicinal and Pharmaceutical  
Chemistry,  
a section of the journal  
Frontiers in Chemistry

**Received:** 02 March 2018

**Accepted:** 30 May 2018

**Published:** 20 June 2018

### Citation:

Tsoukalas C, Psimadas D, Kastis GA, Koutoulidis V, Harris AL, Paravatou-Petsotas M, Karageorgou M, Furenlid LR, Mouloupoulos LA, Stamopoulos D and Bouziotis P (2018) A Novel Metal-Based Imaging Probe for Targeted Dual-Modality SPECT/MR Imaging of Angiogenesis. *Front. Chem.* 6:224. doi: 10.3389/fchem.2018.00224

<sup>1</sup> Radiochemical Studies Laboratory, Institute of Nuclear & Radiological Sciences & Technology, Energy & Safety, National Center for Scientific Research "Demokritos," Athens, Greece, <sup>2</sup> Research Center of Mathematics, Academy of Athens, Athens, Greece, <sup>3</sup> First Department of Radiology, School of Medicine, National and Kapodistrian University of Athens, Athens, Greece, <sup>4</sup> Weatherall Institute of Molecular Medicine, University of Oxford, Oxford, United Kingdom, <sup>5</sup> Department of Solid State Physics, National and Kapodistrian University of Athens, Athens, Greece, <sup>6</sup> Department of Medical Imaging, Center for Gamma-Ray Imaging, University of Arizona, Tucson, AZ, United States, <sup>7</sup> College of Optical Sciences, University of Arizona, Tucson, AZ, United States, <sup>8</sup> Institute of Nanoscience and Nanotechnology, National Center for Scientific Research "Demokritos," Athens, Greece

Superparamagnetic iron oxide nanoparticles with well-integrated multimodality imaging properties have generated increasing research interest in the past decade, especially when it comes to the targeted imaging of tumors. Bevacizumab (BCZM) on the other hand is a well-known and widely applied monoclonal antibody recognizing VEGF-A, which is overexpressed in angiogenesis. The aim of this proof-of-concept study was to develop a dual-modality nanopatform for *in vivo* targeted single photon computed emission tomography (SPECT) and magnetic resonance imaging (MRI) of tumor vascularization. Iron oxide nanoparticles (IONPs) have been coated with dimercaptosuccinic acid (DMSA), for consequent functionalization with the monoclonal antibody BCZM radiolabeled with <sup>99m</sup>Tc, via well-developed surface engineering. The IONPs were characterized based on their size distribution, hydrodynamic diameter and magnetic properties. *In vitro* cytotoxicity studies showed that our nanoconstruct does not cause toxic effects in normal and cancer cells. Fe<sub>3</sub>O<sub>4</sub>-DMSA-SMCC-BCZM-<sup>99m</sup>Tc were successfully prepared at high radiochemical purity (>92%) and their stability in human serum and in PBS were demonstrated. *In vitro* cell binding studies showed the ability of the Fe<sub>3</sub>O<sub>4</sub>-DMSA-SMCC-BCZM-<sup>99m</sup>Tc to bind to the VEGF-165 isoform overexpressed on M-165 tumor cells. The *ex vivo* biodistribution studies in M165 tumor-bearing SCID mice showed high uptake in liver, spleen, kidney and lungs. The Fe<sub>3</sub>O<sub>4</sub>-DMSA-SMCC-BCZM-<sup>99m</sup>Tc demonstrated quick tumor accumulation starting at 8.9 ± 1.88%ID/g at 2 h p.i., slightly increasing at 4 h p.i. (16.21 ± 2.56%ID/g) and then decreasing at 24 h p.i. (6.01 ± 1.69%ID/g). The tumor-to-blood ratio reached a maximum at 24 h p.i. (~7), which is also the case for the tumor-to-muscle ratio (~18). Initial pilot imaging studies on an experimental gamma-camera

and a clinical MR camera prove our hypothesis and demonstrate the potential of  $\text{Fe}_3\text{O}_4$ -DMSA-SMCC-BCZM- $^{99\text{m}}\text{Tc}$  for targeted dual-modality imaging. Our findings indicate that  $\text{Fe}_3\text{O}_4$ -DMSA-SMCC-BCZM- $^{99\text{m}}\text{Tc}$  IONPs could serve as an important diagnostic tool for biomedical imaging as well as a promising candidate for future theranostic applications in cancer.

**Keywords:** SPECT/MRI, bevacizumab, iron oxide nanoparticles, angiogenesis, dual-modality imaging

## INTRODUCTION

Through the last two decades researchers have introduced many innovations in the area of imaging and therapy. Nanoparticles (NPs) with or without conjugated target moieties have proven invaluable tools in cancer research for multimodal imaging and targeted drug delivery as well as hyperthermia and/or controlled release treatment (Lee and Chen, 2009; Bouziotis et al., 2013). More specifically, magnetite NPs (IONPs) such as iron oxide NPs have many advantages such as their controlled size, their facile chemical modification and their ability to be manipulated by an external magnetic field, resulting in a specific, topical accumulation of IONPs and a consequent T2-enhanced MRI signal. Development of such novel imaging tools bearing optimized imaging characteristics can lead to early diagnosis and thus improved patient management.

Nanotechnology-based drug delivery platforms have emerged as a “complete system” for cancer diagnosis and therapy. More specifically, NP-based drug delivery systems can improve solubility and circulation time of therapeutic agents, resulting in overcoming limitations e.g., poor pharmacokinetics, relative to conventional drug formulations (van Vlerken and Amiji, 2006; Anselmo and Mitragotri, 2016). The enhanced permeability and retention (EPR) effect is of great importance, because it can “drive” NP systems to accumulate in the disease site by extravasation through leaky blood vessels (Torchilin, 2014). However, this passive diffusion is not enough for selective nanoparticle uptake in cancer cells (Bertrand et al., 2014).

The ability of nanoparticles to effectively travel across the tumor vessel wall to the interstitial space depends on the ratio of particle size to the size of the openings (Chauhan et al., 2012). On one hand, if this ratio is small, the transport of the particle through the pores of the wall is unhindered. On the other hand, if the size of the nanoparticle is comparable to the size of the openings, the particle will interact with the pores and the transport might be severely hindered. Moreover, large nanoparticles (>40 nm in diameter) even if they manage to cross the vessel wall, they might not be able to penetrate the dense extracellular matrix of the tumor interstitial space (Pluen et al., 2001). Indeed in many tumors, a desmoplastic response might occur that can lead to excessive production of extracellular fibers resulting in limited penetration of nanoparticles (Chauhan et al., 2011).

Following another approach, and in order to overcome these problems, NPs have been conjugated/complexed with various targeting moieties (e.g., small molecules, antibodies, peptides, and aptamers) leading to increased retention and accumulation

in the tumor vasculature as well as selective and efficient internalization by target tumor cells (Zhong et al., 2014). These active targeting NP platforms achieve superior specificity, providing enhanced imaging and/or therapeutic performances compared to their passive targeting analogues.

As far as diagnostic imaging is concerned, it is not feasible to obtain all the necessary information for a particular system from a single imaging modality (De Rosales et al., 2011; Lee et al., 2014). The radionuclide-based SPECT (single photon emission computed tomography) or PET (positron emission tomography) imaging techniques offer high sensitivity but poor resolution, while MRI offers high-resolution anatomical information, but suffers from low sensitivity. Using these combinations, imaging scanners nowadays are capable of providing molecular and physiological information with remarkable sensitivity using PET and SPECT radiotracers and, at the same time, anatomical information of the tissues of interest. A hybrid SPECT/MRI probe: a) has the potential to provide better probe concentration quantification from the acquired SPECT signal, and higher spatial resolution from MRI contrast, thus leading to images that offer more relevant biological information than could be acquired from either imaging modality alone (Hoffman et al., 2014) and can highlight the value of validating different imaging methods against one another. Thus, the combination of SPECT/MRI or PET/MRI can offer synergistic advantages and lead to the more accurate *in vivo* interpretation of disease and abnormalities.

Dual modality contrast agents have already started making their mark in medical imaging. The combination of PET/SPECT with MRI can offer synergistic advantages for sensitive, high-resolution, and quantitative imaging, which can lead to the more accurate, noninvasive interpretation of disease and abnormalities and early detection of various diseases e.g., cancer (Ai et al., 2016).

Simultaneous optical and MR imaging of cancers was recently investigated by labeling recombinant humanized monoclonal antibodies or high-affinity small peptides against tumor receptors, which serve as targeting ligands, with near infrared dyes, and conjugating them to MNPs for simultaneous optical and MR imaging of cancers (Lin et al., 2018). Additionally, peptide-modified gadolinium oxide nanoprobe containing fluorescein for targeted MR/optical dual-modality imaging of various cancers have been engineered (Cui et al., 2017). Live-cell imaging studies suggest that amphiphilic dual-modality nanoprobe, containing a fluorophore for optical imaging and a metal ion chelator complexed with Gd for MRI, can self-assemble into supramolecular nanostructures and effectively label cells (Liu et al., 2015). The formation of new blood vessels

*de novo* (vasculogenesis) normally occurs in fetus and in uterus assuring the supply of nutrients and oxygen to proliferating tissues (Carmeliet, 2005). However, the formation of new blood vessels from pre-existing ones (angiogenesis) is also critical in the development of various disorders including cancer, wound healing and inflammation (Eliceiri and Cheresch, 1999). As far as carcinogenesis is concerned many molecules and receptors are involved in angiogenesis regulation providing important targets for tumor diagnosis and therapy. Vascular endothelial growth factor (VEGF) is a signal protein that stimulates angiogenesis, which can contribute to tumorigenesis when it is overexpressed. The VEGF family of glycoproteins comprises five members, with the VEGF-A being the essential one for the growth and metastasis of tumors. The recombinant humanized monoclonal antibody Bevacizumab (BCZM) is an angiogenesis inhibitor that blocks angiogenesis by binding to VEGF-A (Los et al., 2007). It was developed from a murine antibody (A 4.6.1) and humanized, while retaining the specificity of the original molecule.

BCZM has been approved for the treatment of a variety of metastatic cancers and can be an ideal molecule that can target tumor sites by VEGF-A targeting (Shih and Lindley, 2006). Even though a lot of research has been performed on *in vivo* NP distribution, only a few studies are available on antibody-targeted NPs (Schroeder et al., 2012; Karmani et al., 2013). In the present study we investigated the efficacy of conjugating BCZM onto IONPs and the radiolabeling of the functionalized nanosystems with  $^{99m}\text{Tc}$ , for imaging VEGF-expressing tumors. The radiolabeled nanoformulations were evaluated *in vitro* as well as *in vivo* in tumor angiogenesis models. Active targeting afforded by  $\text{Fe}_3\text{O}_4$ -DMSA-SMCC-BCZM- $^{99m}\text{Tc}$  was evaluated in M165 tumor-bearing mice, in comparison to the non-specific  $\text{Fe}_3\text{O}_4$ -DMSA- $^{99m}\text{Tc}$  IONPs. In order to prove the efficacy of the targeted approach, preliminary imaging studies on tumor-bearing animals using MRI and gamma-ray scintigraphy were performed, which demonstrate the potential of  $\text{Fe}_3\text{O}_4$ -DMSA-SMCC-BCZM- $^{99m}\text{Tc}$  for targeted dual-modality imaging.

## MATERIALS AND METHODS

### Chemicals

All chemicals were reagent grade and were used as such unless otherwise noted. Iron(II) chloride tetrahydrate ( $\text{FeCl}_2 \cdot 4\text{H}_2\text{O}$ , Reagent Plus, 99%) and iron(III)chloride ( $\text{FeCl}_3$ , reagent grade, 97%) were purchased from Sigma-Aldrich. Analytical grade  $\text{NH}_4\text{OH}$  was purchased from AnalytiCals (Carlo Erba). Purified deionized water was prepared by the Milli-Q system (Millipore Co., Billerica, MA, USA). Technetium-99m, in the form of  $\text{Na}^{99m}\text{TcO}_4$  in physiological saline, was eluted from a commercial  $^{99}\text{Mo}/^{99m}\text{Tc}$  generator acquired from GE Healthcare Ltd (United Kingdom). The monoclonal antibody Bevacizumab (Avastin<sup>®</sup>) was purchased from Roche (United Kingdom). Sulfo-SMCC (sulfosuccinimidyl 4-(N-maleimidomethyl)cyclohexane-1-carboxylate) was purchased from Thermo Fischer Scientific, while *meso*-2,3-Dimercaptosuccinic acid and human serum were acquired from Sigma-Aldrich (St. Louis, MO, USA). The human embryonic kidney cell line HEK293 was acquired from the American Type Culture Corporation, while the MDA MB 231

breast cancer cells transfected with the VEGF-165 isoform (M165) were donated by Cancer Research UK. For cell culturing, Dulbecco's modified Eagle medium (DMEM), fetal bovine serum (FBS), penicillin/streptomycin, L-glutamine, and trypsin/EDTA solution were purchased from PAA Laboratories (GmbH, Austria). The MTT tetrazolium salt, (3-[4,5-dimethylthiazol-2-yl)-2,5-diphenyltetrazolium bromide, was acquired from Thermo Fisher Scientific (Cat. No. M6494).

### Equipment

Radioactivity of the  $\text{TcO}_4^-$  eluent was measured using a dose calibrator (Capintec, Ramsey, NJ). Thin-layer chromatography (TLC) silica gel 60 sheets ( $5 \times 10$  cm) were purchased from Merck (Darmstadt, Germany) and along with a Radio-TLC Scanner (Scan-Ram, LabLogic, Sheffield, UK) were used in the determination of radiolabeling yield/purity and *in vitro* stability studies. Radiolabeling yield of the radiolabeled antibody was assessed by HPLC (Waters). PD-10 columns (GE Healthcare), containing Sephadex G-25 resin, were used for the purification of the mercaptoethanol-reduced monoclonal antibody, while Amicon filters (cut-off value: 100 kD) were used for purification of the radiolabeled antibody. Water was deionized to  $18 \text{ M}\Omega \cdot \text{cm}$  using an easy-pure water filtration system (Barnstead International, Dubuque, Iowa). A gamma scintillation counter, a Packard Cobra II, was used to measure the radioactivity of each organ and blood samples in *ex vivo* biodistribution studies. An AXIOS-150/EX (Triton Hellas) dynamic light scattering (DLS) apparatus equipped with a 30 mW He-Ne laser emitting at 658 nm and an Avalanche photodiode detector at an angle of  $90^\circ$  was used for the determination of the size distributions of the nanoparticles.

Planar Scintigraphy studies were performed on a compact, high-resolution, gamma-ray camera developed at the Center for Gamma-Ray Imaging of the University of Arizona. Details of the system can be found elsewhere (Furenlid et al., 2004, 2005; Chen et al., 2005). The system comprises a 5-mm thick NaI(Tl) scintillation crystal, a 12-mm thick quartz light guide, a  $3 \times 3$  array of 1.5-inch diameter photomultiplier tubes (PMTs), and a 40-mm thick lead parallel-hole collimator with hexagonal holes 1 mm in diameter. The system achieves a spatial resolution of about 2.5 mm at the collimator. The field-of-view of the camera is  $4.0 \times 4.0$  in, enough to image a whole mouse without any translation.

MRI studies were performed on a 3 Tesla MRI Unit (Philips Ingenia, Philips Medical Systems, Best, The Netherlands).

### Experimental

#### Synthesis of $\text{Fe}_3\text{O}_4$ IONPs

Superparamagnetic iron oxide nanoparticles (IONPs) were synthesized in-house, according to a previously reported procedure by mixing 40.5 mg (0.25 mmol) anhydrous  $\text{FeCl}_3$  (MW 160.20) and 49.7 mg (0.25 mmol)  $\text{FeCl}_2 \cdot 4\text{H}_2\text{O}$  (MW 198.81) in ultrapure water (Stamopoulos et al., 2007). Subsequently, the complete precipitation of the IONPs was achieved by the abrupt addition of 1.5 ml of a solution of  $\text{NH}_4\text{OH}$  ( $\text{NH}_4\text{OH}:\text{H}_2\text{O}$  1:2) to the suspension (pH 9-9.5). The vials were immediately sealed, to avoid exposure to atmospheric

O<sub>2</sub> and were intensely stirred. The solution was subjected to magnetic decantation followed by repeated washing with distilled water (pH 6.5).

### Functionalization of IONPs With DMSA

Fe<sub>3</sub>O<sub>4</sub> IONPs (1.0 mL, 0.008 mmol) were incubated with 0.027 mmol DMSA dissolved in 1 mL DMSO and left overnight on a stirring apparatus at RT. The supernatant was then removed by magnetic retraction of the NP-DMSA, the nanoconjugate was washed thrice with deionized water and then reconstituted in 1 mL ultrapure water.

### Conjugation of BCZM to NP-DMSA

Sulfosuccinimidyl-4-(N-maleimidomethyl)cyclohexane-1-carboxylate (Sulfo-SMCC) was used as the crosslinker between the NP-DMSA and BCZM. For conjugation of the antibody with the crosslinker, 50  $\mu$ L of sulfo-SMCC (4.8 mg/mL in H<sub>2</sub>O) were added to an aliquot containing  $\sim$ 500  $\mu$ g (0.003  $\mu$ mol in 1 mL PBS) BCZM. The reaction mixture was incubated for 30 min at RT. The excess crosslinker was removed by centrifugation, using an Amicon filter with a 100 kD cut-off value. The purified SMCC-BCZM was then added to 1 mL NP-DMSA and incubated for 30 min at RT, under mechanical stirring. The supernatant was then removed by magnetic retraction of the NP-DMSA-SMCC-BCZM, the nanoconjugate was washed thrice with deionized water and then reconstituted in 1 mL deionized water, for further use in characterization and cytotoxicity experiments.

### Size Analysis of Fe<sub>3</sub>O<sub>4</sub>, Fe<sub>3</sub>O<sub>4</sub>-DMSA and Fe<sub>3</sub>O<sub>4</sub>-DMSA-SMCC-BCZM IONPs

Dynamic light scattering (DLS) was used to measure the size distributions of Fe<sub>3</sub>O<sub>4</sub>, Fe<sub>3</sub>O<sub>4</sub>-DMSA and Fe<sub>3</sub>O<sub>4</sub>-DMSA-SMCC-BCZM nanoparticles in aqueous solutions using a DLS apparatus.

In a typical DLS measurement, 100  $\mu$ L of Fe<sub>3</sub>O<sub>4</sub> IONPs (1.25 mg/ml) diluted with 400  $\mu$ L ultrapure water were measured at 22°C. Furthermore, 2 mg of Fe<sub>3</sub>O<sub>4</sub>-DMSA IONPs diluted with 800  $\mu$ L ultrapure water and 0.1 mg of Fe<sub>3</sub>O<sub>4</sub>-DMSA-SMCC-BCZM NPs diluted with 400  $\mu$ L ultrapure water were also measured at 22°C. For each dispersion, at least 10 light scattering measurements were collected and the results were averaged.

### Magnetic Properties of Fe<sub>3</sub>O<sub>4</sub>, Fe<sub>3</sub>O<sub>4</sub>-DMSA and Fe<sub>3</sub>O<sub>4</sub>-DMSA-SMCC-BCZM IONPs

Magnetic measurements of Fe<sub>3</sub>O<sub>4</sub>, Fe<sub>3</sub>O<sub>4</sub>-DMSA and Fe<sub>3</sub>O<sub>4</sub>-DMSA-SMCC-BCZM powder samples were carried out by means of a SQUID magnetometer (5.5 T MPMS, Quantum Design). Magnetization vs. magnetic field, M(H) was performed both at  $T = 300$  K and  $T = 10$  K, while magnetization vs. temperature, M(T), was measured at  $H = 50$  Oe in both the zero-field cooling (ZFC) and field cooling (FC) modes (ZFC: cooling the sample to the desired temperature under zero magnetic field and then starting measuring its magnetization while progressively increasing the temperature; FC: cooling the sample to the desired temperature under the presence of a specified magnetic field while simultaneously measuring its magnetization).

### Antibody Conjugation

UV-Vis spectrophotometry was used to evaluate the conjugation between Fe<sub>3</sub>O<sub>4</sub>-DMSA and SMCC-BCZM. All samples were prepared by addition of SMCC-BCZM to Fe<sub>3</sub>O<sub>4</sub>-DMSA, intense vortexing for 1 min and consequent shaking for 30 min at RT. To a stable concentration of Fe<sub>3</sub>O<sub>4</sub>-DMSA (3 mmol/L), different concentrations of SMCC-BCZM were added, ranging from 0.0625 to 0.75 mg/mL. BCZM concentration was measured in the supernatant, after magnetic retraction of the nanoparticles. A reference BCZM solution ( $C = 1$  mg/mL) was used in the control experiment, i.e., in the absence of nanoparticles.

### In Vitro Cytotoxicity Study of Fe<sub>3</sub>O<sub>4</sub>-DMSA-SMCC-BCZM IONPs

Two epithelial cell lines were used for the evaluation of cytotoxicity of Fe<sub>3</sub>O<sub>4</sub>-DMSA-SMCC-BCZM IONPs, namely HEK293T (ATCC CRL-3216) and MDA MB 231 breast cancer cells transfected with the VEGF-165 isoform (M165). HEK293 cells are used as the control group (non-cancerous cell line) in our experiments. Both cell lines were cultured in standard DMEM complete (10% FBS, 1% penicillin/streptomycin, 1% L-glutamine). Cells were incubated at 37°C in a humidified atmosphere of 5% CO<sub>2</sub>.

### MTT Assay

As a general protocol, 5,000 cells/well were seeded in 96-well plates (Corning-Costar, Corning, NY) and cultured overnight. The positive control of this study had cells with culture medium, which were not exposed to IONPs. The two different cell lines were treated with various concentrations of Fe<sub>3</sub>O<sub>4</sub>-DMSA-SMCC-BCZM IONPs (3, 5, 10, 20, 25, 30, 35, 40, 45, 50, 100, 200, 500, and 1,000  $\mu$ g/ml) for 24 h. Subsequently, the cells were rinsed once and incubated at 37°C with 100  $\mu$ l serum-free medium, containing 0.5 mg/mL MTT. After 2 h, 100  $\mu$ l of SDS-HCl was added to each well, mixed with the pipette and incubated for at least 1 h at 37°C. The optical densities were read at 570 nm (reference filter was set at 690 nm), on an ELISA reader.

### Radiolabeling of Fe<sub>3</sub>O<sub>4</sub> IONPs With Technetium-99m

#### Radiolabeling of Fe<sub>3</sub>O<sub>4</sub>-DMSA With Technetium-99m: Passive Delivery of Nanoparticles

Radiolabeling of Fe<sub>3</sub>O<sub>4</sub>-DMSA with <sup>99m</sup>Tc was performed *via* the precursor <sup>99m</sup>Tc-gluconate, as follows: A solid mixture containing 1.0 g Na gluconate, 2.0 g NaHCO<sub>3</sub> and 0.015 g SnCl<sub>2</sub> was homogenized and kept dry. A quantity of 0.003 g of the above mixture was dissolved in 1.0 ml of a Na<sup>99m</sup>TcO<sub>4</sub> solution, containing 370 MBq (10 mCi) of <sup>99m</sup>Tc (Varvarigou et al., 2002). An aliquot of the above solution (100  $\mu$ L) containing  $\sim$ 37 MBq of the reduced <sup>99m</sup>Tc was added to 8  $\mu$ mol Fe<sub>3</sub>O<sub>4</sub>-DMSA. The mixture was left at RT and the exchange reaction was completed in 30 min. The radiolabeling yield was determined by thin layer chromatography analysis (TLC). ITLC-SG was used as the stationary phase. The strips were developed using MEK and a 3/5/1.5 mixture pyridine/acetic acid/H<sub>2</sub>O as the mobile phases, to determine free pertechnetate, <sup>99m</sup>TcO<sub>2</sub> and Fe<sub>3</sub>O<sub>4</sub>-DMSA-<sup>99m</sup>Tc. With MEK, pertechnetate ions migrate with the solvent front,

while in pyridine/acetic acid/H<sub>2</sub>O <sup>99m</sup>TcO<sub>2</sub> remains at the spot and Fe<sub>3</sub>O<sub>4</sub>-DMSA-<sup>99m</sup>Tc migrates to the front. The radiolabeled sample was purified by magnetic retraction. After washing twice with deionized water, the supernatant was removed and the radiolabeled sample was redispersed in deionized water. The % radiochemical purity of Fe<sub>3</sub>O<sub>4</sub>-DMSA-<sup>99m</sup>Tc was determined by TLC, as previously described. A control test was also carried out, in the absence of Fe<sub>3</sub>O<sub>4</sub>-DMSA-<sup>99m</sup>Tc.

### Radiolabeling of BCZM With <sup>99m</sup>Tc and Consequent Conjugation to Fe<sub>3</sub>O<sub>4</sub>-DMSA: Active Targeting of VEGF-A Expression

BCZM-SMCC was prepared as described above. Thereafter, in order to adequately prepare BCZM for consequent radiolabeling with <sup>99m</sup>Tc, its endogenous disulfide bonds were partially reduced with 2-mercaptoethanol. Briefly, BCZM-SMCC (500 μL, C<sub>Ab</sub> = 2.5 mg/mL) was incubated with 25 μL 2-mercaptoethanol (1,000:1 molar ratio) for 30 min at RT. The reduced antibody conjugate was purified by centrifugation (12,000 rpm, 10 min, AMICON filters MWCO: 100kD) and reconstituted in deionized water. Labeling of BCZM-SMCC was afforded by the addition of the <sup>99m</sup>Tc-gluconate precursor (100 μL/37 MBq) (Varvarigou et al., 1996). The radiolabeling yield was determined by HPLC performed on a Waters HPLC system using a TSKgel G3000SWXL size exclusion column (TOSOH Bioscience, Germany). As the eluent, PBS pH 7.4 was used at a flow rate of 0.8 mL/min. Finally, <sup>99m</sup>Tc-BCZM-SMCC was added to 8 μmol Fe<sub>3</sub>O<sub>4</sub>-DMSA, intensely vortexed for 1 min, and shaken at RT for 30 min on a mechanical shaker. The radiolabeled sample was purified by magnetic retraction. After washing thrice with deionized water, the supernatant was removed and the radiolabeled sample was redispersed in 1 mL deionized water. The % radiochemical purity of Fe<sub>3</sub>O<sub>4</sub>-DMSA-SMCC-BCZM-<sup>99m</sup>Tc IONPs was determined by TLC, as previously described. A control test was also carried out, in the absence of IONPs.

### In Vitro Stability Studies of Fe<sub>3</sub>O<sub>4</sub>-DMSA and Fe<sub>3</sub>O<sub>4</sub>-DMSA-SMCC-BCZM-<sup>99m</sup>Tc IONPs

To evaluate the *in vitro* stability of Fe<sub>3</sub>O<sub>4</sub>-DMSA-<sup>99m</sup>Tc and Fe<sub>3</sub>O<sub>4</sub>-DMSA-SMCC-BCZM-<sup>99m</sup>Tc, 10 μL samples of each of the radiolabeled nanoconjugates were incubated with 90 μL phosphate buffer saline (PBS) pH 7.4 while shaking at RT. For serum stability studies, 50 μL of each of the radiolabeled nanoconjugates were incubated with 450 μL human serum at 37°C. *In vitro* stability was determined at four time points (1, 2, 4, and 24 h) by TLC, as described above. All experiments were performed in triplicate.

### In Vitro Cell Binding Assay

*In vitro* cell binding experiments were performed on M165 cells, in order to assess the targeting capability of both BCZM-functionalized Fe<sub>3</sub>O<sub>4</sub>-DMSA-SMCC-BCZM-<sup>99m</sup>Tc and non-functionalized Fe<sub>3</sub>O<sub>4</sub>-DMSA-<sup>99m</sup>Tc (Orocio-Rodríguez et al., 2015; Mendoza-Nava et al., 2016). Cells were cultured as described above for the cytotoxicity experiment. On the day prior to experiments, M165 cells were seeded in 24-well plates and grown to confluency. For the binding experiment, 50 μL

(0.4 μmol) of either nanoconstruct were added to each well and incubated for 1 h at 37°C. Subsequently the supernatant was removed, the cells were washed 3 times with ice-cold PBS and lysed by the addition of 1 M NaOH. Activity was measured, along with an aliquot with the initial activity, representing 100% added activity. The percent cell uptake was then calculated. Non-specific binding was determined in parallel, in the presence of a large excess of unlabeled BCZM, with 1 h of pre-incubation.

### Ex Vivo Biodistribution Studies of Bare (Fe<sub>3</sub>O<sub>4</sub>-DMSA-<sup>99m</sup>Tc) and Antibody-Functionalized (Fe<sub>3</sub>O<sub>4</sub>-DMSA-SMCC-BCZM-<sup>99m</sup>Tc) IONPs

Animal experiments were carried out according to European and national regulations. These studies have been further approved by the Ethics Committee of the NCSR “Demokritos” and animal care and procedures followed are in accordance with institutional guidelines and licenses issued by the Department of Agriculture and Veterinary Policies of the Prefecture of Attiki (Registration Numbers: EL 25 BIO 022 and EL 25 BIO 021). Immunodeficient SCID mice were obtained from the breeding facilities of the Institute of Biosciences and Applications, NCSR “Demokritos.” The animals were housed in air-conditioned rooms under a 12-h light/dark cycle and allowed free access to food and water.

For the development of experimental tumor models, female SCID mice of 8 weeks on the day of inoculation were subcutaneously inoculated with M165 cells (1 × 10<sup>7</sup> cells). Approximately 2 weeks after inoculation, *ex vivo* biodistribution studies and *in vivo* imaging studies on the tumor-bearing mice were performed. Fe<sub>3</sub>O<sub>4</sub>-DMSA-<sup>99m</sup>Tc and Fe<sub>3</sub>O<sub>4</sub>-DMSA-SMCC-BCZM-<sup>99m</sup>Tc were evaluated in 2 groups of tumor-bearing SCID mice (*n* = 4 mice, animal weight 18–20 g). The nanoradiotracers were intravenously administered via the tail vein. Each mouse received 100 μL (0.8 μmol/89 μg/2.0 ± 0.3 MBq) of either Fe<sub>3</sub>O<sub>4</sub>-DMSA-<sup>99m</sup>Tc (passive delivery) or Fe<sub>3</sub>O<sub>4</sub>-DMSA-SMCC-BCZM-<sup>99m</sup>Tc (active targeting). The animals were euthanized at 2, 4, and 24 h post-injection (4 mice per time-point) and the organs of interest, as well as the tumor, were removed, weighed and counted in a NaI well-counter, along with samples of blood, muscles and urine. The remaining radioactivity in the tail, as well as background counts were subtracted, and the radioactivity decay was auto-corrected by the counter. The accumulation of radiolabeled MNPs in each organ was expressed as the percentage injected dose per gram of tissue (%ID/g ± SD) and calculated compared to the activities of a standard dose of the injected solution.

Binding specificity of Fe<sub>3</sub>O<sub>4</sub>-DMSA-SMCC-BCZM-<sup>99m</sup>Tc (the targeted nanoconstruct) was assessed in M165 tumor-bearing mice (*n* = 4 mice), after pre-injection of the mice with 2.5 mg (0.016 μmol)/100 μL “cold” bevacizumab 24 h before injection of the radiotracer. These animals were euthanized at 4 h post-injection of Fe<sub>3</sub>O<sub>4</sub>-DMSA-SMCC-BCZM-<sup>99m</sup>Tc and were assessed as described above.

### In Vivo Imaging Studies (Pilot Studies) Gamma Camera

All animals were bearing a tumor in their left front limb. After tracer injection, the animals were anesthetized with an

intraperitoneal (IP) injection of ketamine (75 mg/kg) and xylazine (5 mg/kg) and placed on the prone position on the camera face. Planar scintigraphy was performed by collecting a 60-min image following tracer injection. Furthermore, all four animals were imaged 24 h after injection by acquiring a 60-min image.

## MR Imaging

MRI exams were conducted at the First Department of Radiology of the National and Kapodistrian University of Athens on a 3 Tesla MRI unit, using a surface phased-array coil.

MRI experiments were performed on 3 groups of M165 tumor-bearing SCID mice, as follows: Group 1: Mice injected with Fe<sub>3</sub>O<sub>4</sub>-DMSA-SMCC-BCZM (1 mg IONPs/100 μL, *n* = 3 mice); Group 2: Mice injected with Fe<sub>3</sub>O<sub>4</sub>-DMSA (1 mg IONPs/100 μL *n* = 3 mice); and Group 3: Mice injected with saline (*n* = 2 mice). Anesthesia was induced with a mixture of ketamine/xylazine. T2-Weighted images were acquired before the injection of nanoparticles. The next day mice were injected with Fe<sub>3</sub>O<sub>4</sub>-DMSA-SMCC and Fe<sub>3</sub>O<sub>4</sub>-DMSA-SMCC-BCZM and were imaged 4 h post-injection with the same parameters. MR images were reviewed and signal intensity measurements were performed on a dedicated workstation using diagnostic software (Philips Intellispace Portal v9, Philips Healthcare, Best, The Netherlands).

## Histopathology Studies

Twenty-four hours post-MRI scanning, the mice were euthanized and the tumors, livers, lungs and kidneys of each mouse were surgically removed. The tissues were then fixed in 10% formalin, embedded in paraffin, sectioned at 6 μm and stained with Perl's reagent (Prussian Blue). The slides and the pictures of each tissue were taken using an Olympus U-TVO.5XC-3 microscope,

equipped with an Infinity1 Lumenera camera (magnification × 40).

## Statistical Analysis

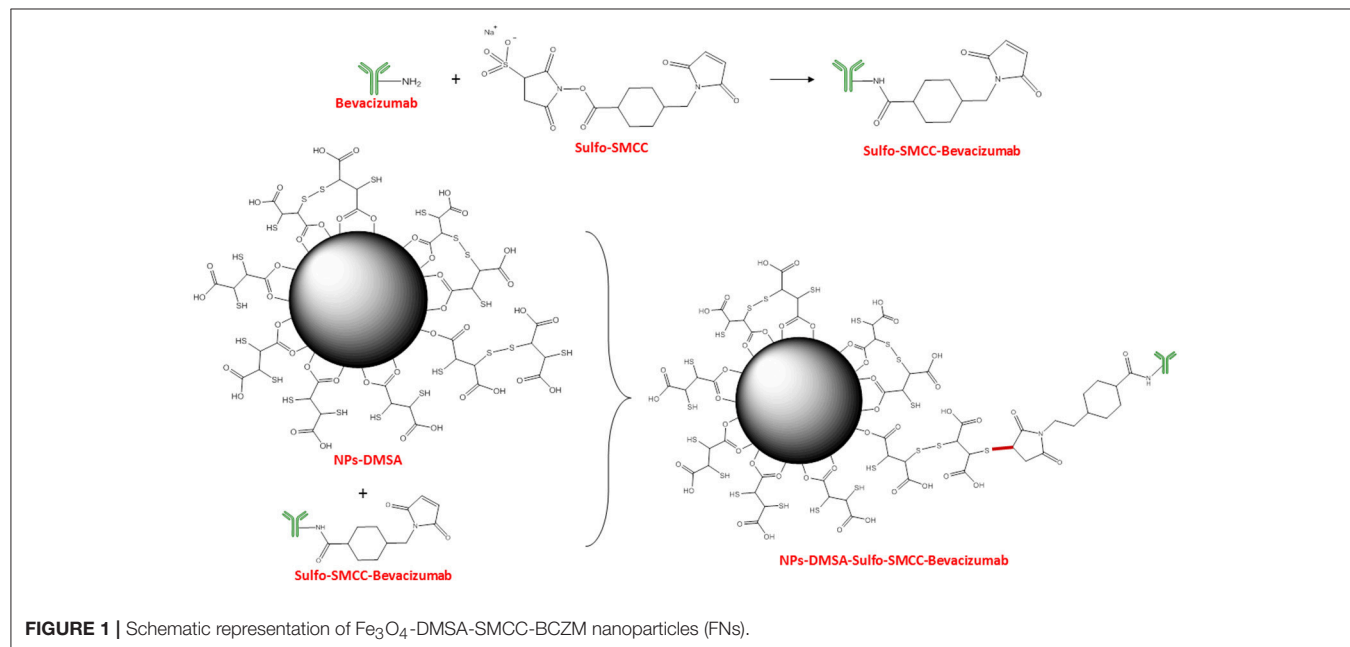
The data are presented as means ± standard deviations. For the biodistribution studies, the data were compared using an unpaired *t*-test with a significance level of *P* < 0.05. All analyses were performed using Microsoft Office Excel.

## RESULTS AND DISCUSSION

The aim of the present study was to show that bevacizumab-functionalized IONPs show specific accumulation in VEGF-A expressing tumors, while their non-functionalized counterparts exhibit limited uptake due to the EPR effect. The primary idea behind the design and synthesis of these NPs was to provide a platform for the development of a dual-modality molecular imaging agent.

## Synthesis and Characterization of Fe<sub>3</sub>O<sub>4</sub> IONPs

The main reason for coating the nanoparticle surface with various molecules is to render them non-toxic, biocompatible and stable (Barrow et al., 2015). 2,3-dimercaptosuccinic acid (DMSA) has been repeatedly used for surface-functionalizing inorganic NPs, as an effective way to increase their biocompatibility (Fauconnier et al., 1997; Auffan et al., 2006; Wang et al., 2011). DMSA is an FDA-approved, orally administered metal-chelating agent often used to coat iron oxide NPs, in order to improve their stability and biocompatibility (Chen et al., 2008). Apart from providing nanoparticle stability under physiological conditions, DMSA offers two functional groups, namely –COOH and –SH, which can both be exploited



for the covalent bonding of a variety of organic molecules (Ruiz et al., 2014; Galli et al., 2017). In this study, IONPs were synthesized according to the co-precipitation method, while their surface was modified with DMSA for further functionalization with BCZM-SMCC (Figure 1). The ligand DMSA binds to the nanoparticle surface in a bidentate manner through oxygen atoms, and the created Fe-O-C bond is similar to a polar covalent bond (Figure 1; Ruiz et al., 2014). Conjugation of BCZM to the thus formed NP-DMSA was accomplished *via* the crosslinker Sulfo-SMCC. Sulfo-SMCC contains an amine-reactive N-hydroxysuccinimide (NHS ester) and a sulfhydryl-reactive maleimide group. The NHS esters of Sulfo-SMCC react with the primary amines of BCZM to form stable amide bonds while the maleimides react with the sulfhydryl groups of NP-DMSA to form stable thioether bonds.

### Size Analysis of Fe<sub>3</sub>O<sub>4</sub>, Fe<sub>3</sub>O<sub>4</sub>-DMSA and Fe<sub>3</sub>O<sub>4</sub>-DMSA-SMCC-BCZM IONPs

DLS measurements were carried out on the Fe<sub>3</sub>O<sub>4</sub>, Fe<sub>3</sub>O<sub>4</sub>-DMSA and Fe<sub>3</sub>O<sub>4</sub>-DMSA-SMCC-BCZM IONPs (Figure 2). The samples were diluted with ultrapure water and measured at 22°C. Using CONTIN analysis of the DLS measurements, the mean size distribution of intensity weighted hydrodynamic radii of Fe<sub>3</sub>O<sub>4</sub>, Fe<sub>3</sub>O<sub>4</sub>-DMSA, and Fe<sub>3</sub>O<sub>4</sub>-DMSA-SMCC-BCZM IONPs were found to be 335, 206, and 281 nm respectively. This result indicates the general effect of surface coating, which prevents the *in vivo* aggregation of the nanoparticles as it provides sufficient electrostatic (and/or steric) repulsion between them and thus, maintains the nanoparticles apart from one another against attractive forces. The hydrodynamic size of Fe<sub>3</sub>O<sub>4</sub>-DMSA and Fe<sub>3</sub>O<sub>4</sub>-DMSA-SMCC-BCZM IONPs is close to the upper size limit (400–500 nm) for the extravasation of nanoparticles into tumor tissues, *via* the EPR effect.

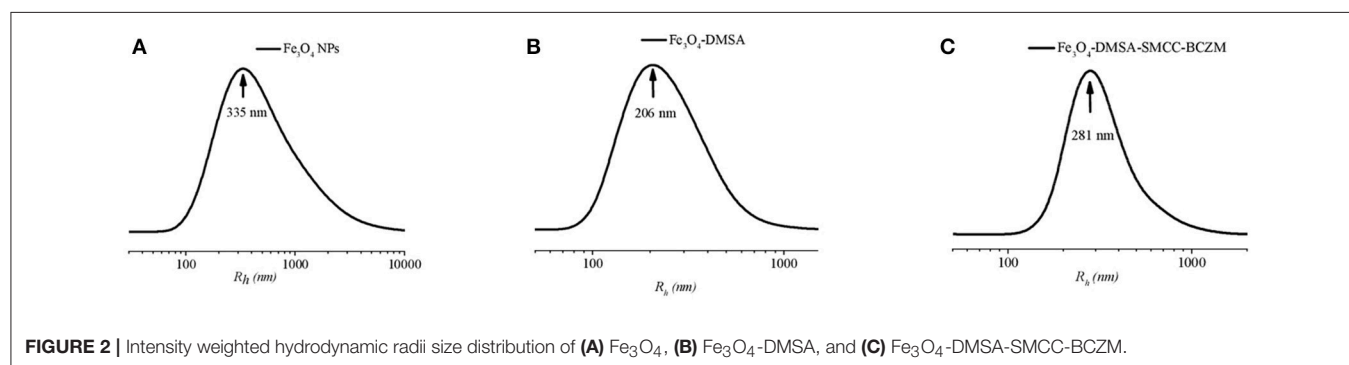
### Magnetic Properties of Fe<sub>3</sub>O<sub>4</sub>, Fe<sub>3</sub>O<sub>4</sub>-DMSA, and Fe<sub>3</sub>O<sub>4</sub>-DMSA-SMCC-BCZM IONPs

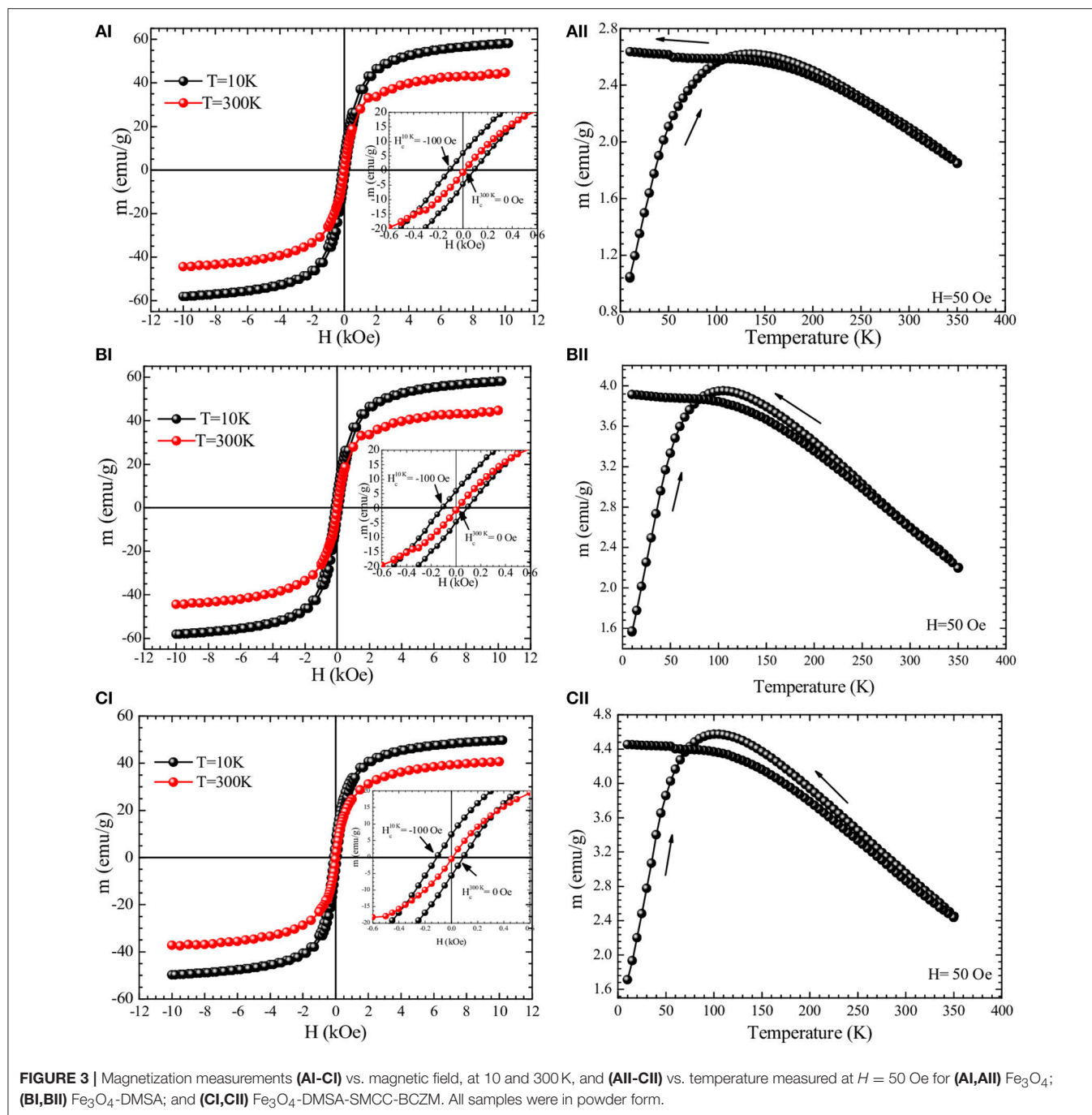
The magnetic properties of Fe<sub>3</sub>O<sub>4</sub>, Fe<sub>3</sub>O<sub>4</sub>-DMSA, and Fe<sub>3</sub>O<sub>4</sub>-DMSA-SMCC-BCZM nanoparticles, presented in Figures 3A–C respectively, were assessed by magnetization measurements vs. magnetic field, M(H), at  $T = 300$  K and  $T = 10$  K [panels (A.I–C.I)], as well as by ZFC-FC magnetization at

50 Oe [panels (A.II–C.II)]. The saturation magnetization,  $M_s$ , was found to be  $M_s = 45$  emu/g,  $M_s = 41$  emu/g and  $M_s = 41$  emu/g at  $T = 300$  K for Fe<sub>3</sub>O<sub>4</sub>, Fe<sub>3</sub>O<sub>4</sub>-DMSA, and Fe<sub>3</sub>O<sub>4</sub>-DMSA-SMCC-BCZM nanoparticles, respectively. From the comparison of the magnetization measurements, it is concluded that the magnetization of all the samples is preserved and is not affected either by the DMSA coating or by the functionalization of the nanoparticles with the antibody. The values of remanent magnetization and coercivity for all samples at 300 K are zero, which is in accordance to their superparamagnetic behavior (or more appropriately, soft ferromagnetic/ferrimagnetic character). Furthermore, the ZFC-FC magnetization curves of Fe<sub>3</sub>O<sub>4</sub>, Fe<sub>3</sub>O<sub>4</sub>-DMSA, and Fe<sub>3</sub>O<sub>4</sub>-DMSA-SMCC-BCZM nanoparticles exhibit a maximum in the ZFC curve that corresponds to the so-called blocking temperature  $T_B = 130$ , 100, and 100 K, respectively. These magnetization data show that the Fe<sub>3</sub>O<sub>4</sub> IONPs preserve their magnetic properties (high saturation magnetization and zero coercivity) upon functionalization and thus are appropriate for usage in diagnostic imaging application at RT.

### Antibody Conjugation

The conjugation between Fe<sub>3</sub>O<sub>4</sub>-DMSA and SMCC-BCZM may be reliably proven by means of UV-vis spectrophotometry, as previously reported by our group (Stamopoulos et al., 2007). Figures 4A,B present data for the supernatant of Fe<sub>3</sub>O<sub>4</sub>-DMSA-SMCC-BCZM samples that were prepared for incubation duration, time = 2 h. (Figure 4A) shows data for constant concentration of Fe<sub>3</sub>O<sub>4</sub> ( $C_{\text{IONPs}} = 3$  mmol/L) and for six different concentrations of BCZM, while (Figure 4B) shows the respective data for constant concentration of BCZM ( $C_{\text{Ab}} = 3$  mmol/L) and six different concentrations of Fe<sub>3</sub>O<sub>4</sub> IONPs. The data of (Figure 4A) clearly show complete conjugation of BCZM to the IONPs for antibody concentrations up to a characteristic value 0.1250 mg/mL. However, the percentage of conjugated BCZM decreases as its initial concentration increases. The data of (Figure 4B) prove that the percentage of BCZM conjugated with the IONPs increases as their concentration increases, however it reaches a plateau at a characteristic value 5 mmol/L. These data guided us to choose an optimum concentration ratio between BCZM and IONPs, that





is  $C_{\text{BCZM}}/C_{\text{IONPs}} = 0.5 \text{ mg/mL}/8 \text{ mmol/L}$ , in our subsequent experiments.

### In Vitro Cytotoxicity Study of $\text{Fe}_3\text{O}_4$ -DMSA-SMCC-BCZM

Cytotoxicity of iron oxide NPs at concentrations  $>300 \mu\text{g/mL}$  is mainly due to the production of Reactive Oxidative Species (ROS) (Shukla et al., 2015). Quantitative assays of the metabolic activity of cancer cell lines in the presence of  $\text{Fe}_3\text{O}_4$ -DMSA-SMCC-BCZM could grant a better knowledge of the mechanisms

implied in the toxicity caused by these IONPs. The MTT viability assay tracks the activity of reductase enzymes, thus measuring the cell viability of M165 and HEK293 cell lines, after a 24 h treatment with various concentrations of  $\text{Fe}_3\text{O}_4$ -DMSA-SMCC-BCZM IONPs (Jarockyte et al., 2016; Karageorgou et al., 2017). Our experiments demonstrated a similar behavior on both the M165 and HEK293 cell lines, at nanoparticle concentrations ranging from 3 to  $1,000 \mu\text{g/mL}$ . Cell viability was over 65% at all concentration points for both cells lines (Figure 5). Keeping in mind that the maximum dose of administered iron oxide

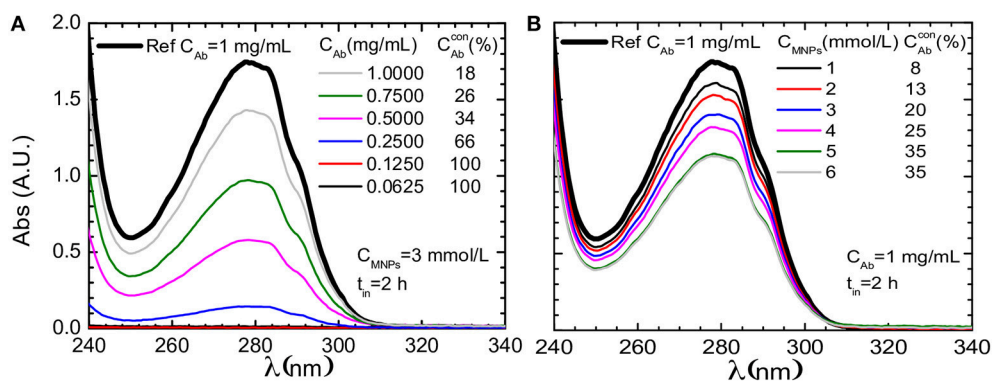


**FIGURE 4** | UV-vis data (focused in the range of 240–340 nm) for the supernatant of  $\text{Fe}_3\text{O}_4$ -DMSA-SMCC-BCZM samples that were prepared for incubation duration, time = 2 h, for six different concentrations of **(A)** BCZM and constant concentration of IONPs ( $C_{\text{FNs}} = 3 \text{ mmol/L}$ ) and **(B)** IONPs and constant concentration of BCZM ( $C_{\text{Ab}} = 3 \text{ mmol/L}$ ). The respective curve of a reference BCZM solution (1 mg/mL) is also shown, in both cases. The  $C_{\text{AB}}^{\text{con}}$  presented in both panels refers to the percentage of BCZM conjugated with the  $\text{Fe}_3\text{O}_4$  IONPs, as this was estimated from the respective set of data. The supernatant of the samples was isolated when the magnetic species were trapped by means of an external magnetic field.

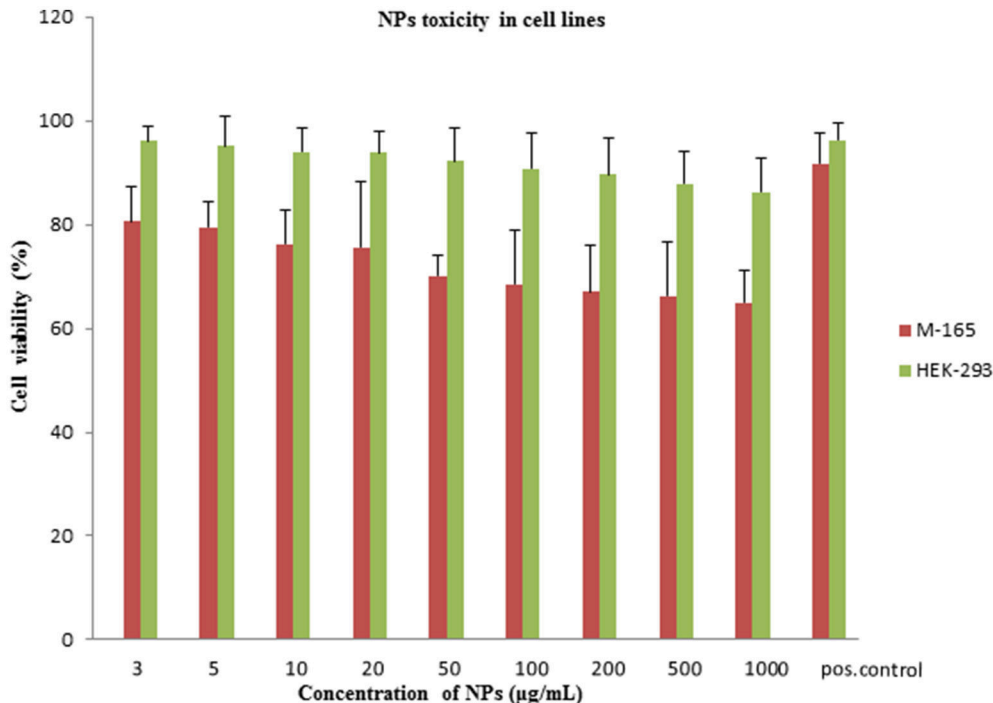


**FIGURE 5** | Viability assay on M165 and HEK293 cell lines. Graph of MTT assay after 24 h treatment of M-165 cells and HEK293 cells with various concentrations of NPs. Positive control shows M-165 cells and HEK293 cells without the exposure to NPs. The cell viability is expressed as % cell viability in comparison to a positive control.

NPs in our study is 1,000  $\mu\text{g}/\text{mouse}$  (which is the injected dose for the MR imaging study), our results suggest that our nanoconstruct does not cause toxic effects on either cell line, even at the 1,000  $\mu\text{g}/\text{ml}$  concentration point. These results are in accordance with toxicity results of other DMSA-coated nanoparticles reported in the literature (Mejías et al., 2010, 2013; Ruiz et al., 2013; Paik et al., 2015; Costa et al., 2016; Shelat et al., 2018).

### Radiosynthesis and *in Vitro* Stability Studies of $\text{Fe}_3\text{O}_4$ -DMSA- $^{99\text{m}}\text{Tc}$ and $\text{Fe}_3\text{O}_4$ -DMSA-SMCC-BCZM- $^{99\text{m}}\text{Tc}$

Radiolabeling of  $\text{Fe}_3\text{O}_4$ -DMSA was achieved by transcomplexation of  $\text{Sn}^{2+}$ -reduced [ $^{99\text{m}}\text{Tc}$ ]-pertechnetate in the presence of an excess of a low-affinity chelating ligand (gluconate), which ensures that  $^{99\text{m}}\text{Tc}$  binds to the exposed thiol groups.  $\text{Fe}_3\text{O}_4$ -DMSA- $^{99\text{m}}\text{Tc}$  was prepared at a

satisfactory radiolabeling yield (70%) and high radiochemical purity (>95%) post-purification by magnetic retraction, as determined by TLC analysis (Figure S1). Labeling of the SMCC-BCZM conjugate was also performed via the  $^{99m}\text{Tc}$ -gluconate precursor at high radiochemical yield (>98%), as determined by HPLC analysis (Figure S2). Incubation of  $\text{Fe}_3\text{O}_4$ -DMSA with SMCC-BCZM- $^{99m}\text{Tc}$  led to the formation of  $\text{Fe}_3\text{O}_4$ -DMSA-SMCC-BCZM- $^{99m}\text{Tc}$  at a radiochemical purity of >92% after purification by magnetic retraction (Figure S3).

A significant factor to be considered when developing a new radiolabeled nanoparticle is that the radionuclide must be bound to the nanoparticle to form a stable conjugate under physiological conditions to avoid their separation and non-specific deposition of free ions in tissues. Otherwise, biodistribution and imaging data will not indicate the fate of nanoparticles, as the radionuclide distribution will not reflect that of the nanoparticles. With the aim to assess the *in vitro* stability of  $\text{Fe}_3\text{O}_4$ -DMSA- $^{99m}\text{Tc}$  and  $\text{Fe}_3\text{O}_4$ -DMSA-SMCC-BCZM- $^{99m}\text{Tc}$  in biological media, the radiolabeled samples were incubated with PBS and human serum. The results exhibited satisfactory *in vitro* stability in PBS (~80% stable IONPs, Figure S4) and high *in vitro* stability human serum (~90% stable IONPs, Figure S5) for both radiotracers at 24 h post-incubation, as evaluated by TLC analysis. From the *in vitro* serum stability results, it is safe to say that both radiolabeled nanoconstructs are stable enough to be used as *in vivo* imaging agents. Our results are in accordance to previously published works (De Rosales et al., 2011; Karageorgou et al., 2017).

### In Vitro Cell Binding Assay

The cell binding assay was performed on the M165 cell line after 24 h incubation with  $\text{Fe}_3\text{O}_4$ -DMSA-SMCC-BCZM- $^{99m}\text{Tc}$  and  $\text{Fe}_3\text{O}_4$ -DMSA- $^{99m}\text{Tc}$  (50  $\mu\text{L}$ , 0.04  $\mu\text{mol}$ ). Targeted  $\text{Fe}_3\text{O}_4$ -DMSA-SMCC-BCZM- $^{99m}\text{Tc}$  had specific recognition, as cell uptake was ~4.3 times higher than for  $\text{Fe}_3\text{O}_4$ -DMSA- $^{99m}\text{Tc}$ , indicating the ability of the immunoconjugate to bind to the VEGF-165 isoform overexpressed on M-165 tumor cells. Specificity of  $\text{Fe}_3\text{O}_4$ -DMSA-SMCC-BCZM- $^{99m}\text{Tc}$  was further confirmed by blocking the cells with an excess of unlabeled BCZM (Table 1; Morales-Avila et al., 2011; Orocio-Rodríguez et al., 2015; Mendoza-Nava et al., 2016).

In light of the performed cell binding studies, and the demonstrated specificity of  $\text{Fe}_3\text{O}_4$ -DMSA-SMCC-BCZM- $^{99m}\text{Tc}$  toward M165 cells overexpressing the VEGF-165 isoform, this

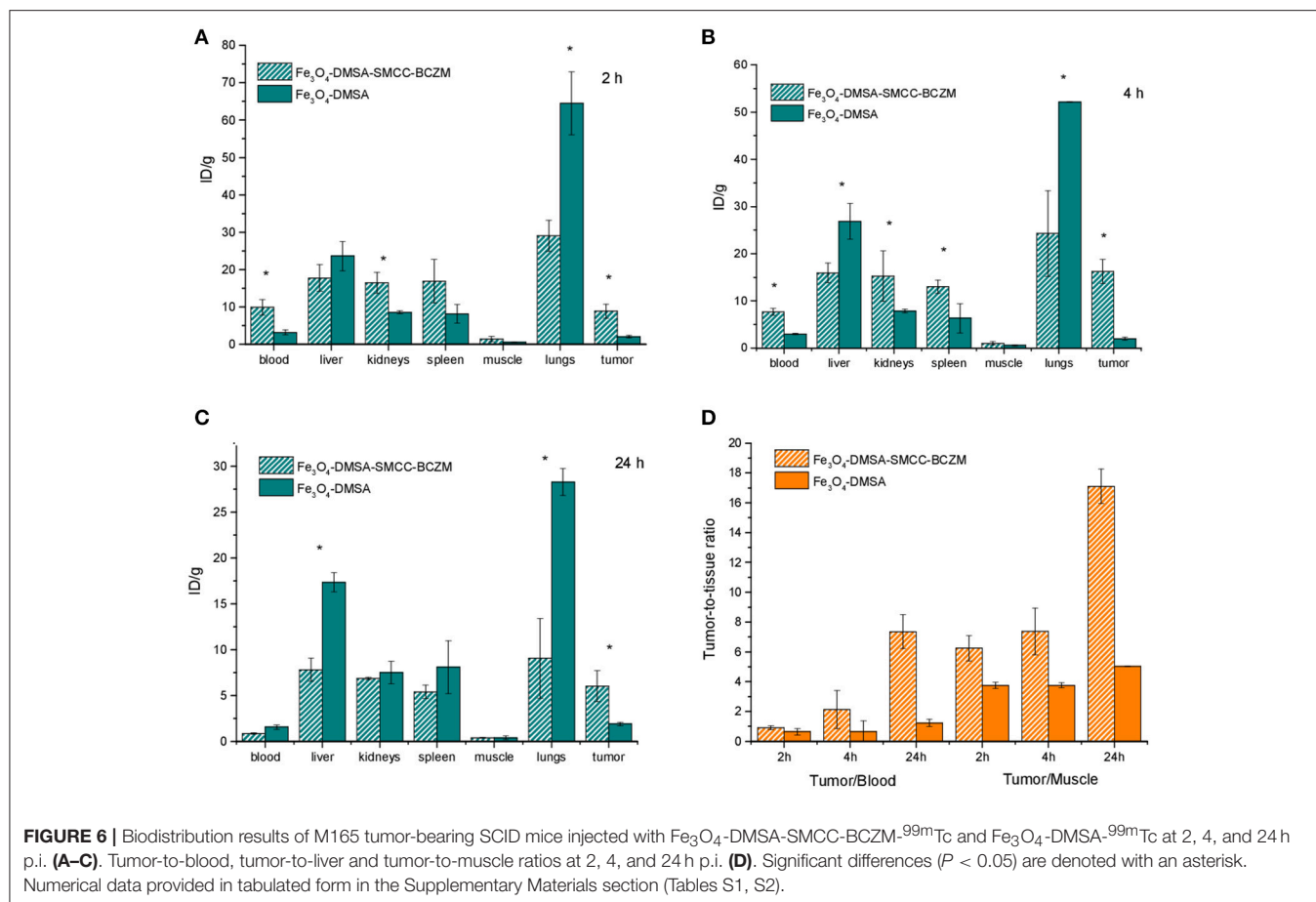
should be the nanoconstruct of choice for further *ex vivo* and *in vivo* experimentation.

### Ex Vivo Biodistribution Studies

In order to evaluate the potential of the radiolabeled NP-systems as SPECT/MRI imaging agents, *ex vivo* biodistribution experiments were performed. Following i.v. injection, the  $^{99m}\text{Tc}$ -labeled ferromagnetic NPs enter the blood stream and after circulating for some time in the body they reach a desired target i.e., tumor, depending on their surface functionalization. The degree of target uptake depends on the affinity between the target molecule and the functionalized NP-system. It is also essential that the administered nanomaterial circulates for long enough time for effective tumor uptake before being eliminated by the organism. The *ex vivo* biodistribution pattern of  $\text{Fe}_3\text{O}_4$ -DMSA- $^{99m}\text{Tc}$  and  $\text{Fe}_3\text{O}_4$ -DMSA-SMCC-BCZM- $^{99m}\text{Tc}$  was assessed in xenografted mice. Both species of IONPs were administered via tail-vein injection in M165 tumor-bearing SCID mice. The accumulation of the technetium-labeled IONPs in the organs at all time-points examined is presented in Figure 6, as percentage of injected dose per gram tissue (% ID/gr  $\pm$  SD). Blood retention of the nanoparticles was  $3.21 \pm 0.65\%$  ID/gr and  $9.90 \pm 2.07\%$  ID/gr at 2 h p.i. for  $\text{Fe}_3\text{O}_4$ -DMSA- $^{99m}\text{Tc}$  and  $\text{Fe}_3\text{O}_4$ -DMSA-SMCC-BCZM- $^{99m}\text{Tc}$ , respectively, while the antibody-functionalized conjugate showed a faster blood clearance at 24 h p.i. ( $0.81 \pm 0.08\%$  ID/gr), compared to the non-functionalized IONPs ( $1.54 \pm 0.24\%$  ID/gr). After organ distribution through blood, high levels of radioactivity were observed for both NPs in liver, spleen, kidney and lungs even, with different kinetics. In the liver, there was more pronounced uptake for  $\text{Fe}_3\text{O}_4$ -DMSA- $^{99m}\text{Tc}$  ( $23.60 \pm 3.90\%$  ID/gr,  $26.84 \pm 3.76\%$  ID/gr and  $17.33 \pm 1.02\%$  ID/gr at 2, 4 and 24 h p.i.), while in the spleen the uptake was considerably lower for both radiolabeled nanoconstructs at 24 h p.i. ( $8.09 \pm 2.88\%$  ID/gr and  $5.38 \pm 0.73\%$  ID/gr, for  $\text{Fe}_3\text{O}_4$ -DMSA- $^{99m}\text{Tc}$  and  $\text{Fe}_3\text{O}_4$ -DMSA-SMCC-BCZM- $^{99m}\text{Tc}$ , respectively). These findings are consistent with the observed faster blood clearance of the non-functionalized IONPs at 2 h p.i., which may be attributed to their rapid accumulation in the liver and lungs. The lower liver uptake for  $\text{Fe}_3\text{O}_4$ -DMSA-SMCC-BCZM- $^{99m}\text{Tc}$  at all the examined time-points ( $17.77 \pm 3.61\%$  ID/gr,  $15.88 \pm 2.10\%$  ID/gr and  $7.81 \pm 1.25\%$  ID/gr at 2, 4 and 24 h p.i.) can be attributed to the presence of BCZM which is protecting them to a certain degree from being recognized by Kupffer cells (de Souza Albernaz et al., 2018). As concluded from the biodistribution studies, the MNP species investigated here are cleared mostly through the hepatobiliary pathway since their hydrodynamic diameter is significantly larger than the cutoff for renal filtration (~5 nm) (Hong et al., 2012). Nevertheless, there is a significant renal uptake at all time-points which can be attributed to a small extent of renal clearance. Additionally, the high radioactivity concentration in the kidneys particularly for  $\text{Fe}_3\text{O}_4$ -DMSA-SMCC-BCZM- $^{99m}\text{Tc}$  at 2 and 4 h p.i. ( $16.46 \pm 2.8\%$  ID/gr and  $15.22 \pm 5.37\%$  ID/gr respectively) can be partly attributed to the expression of VEGF-A in glomerular podocytes and in tubular epithelial cells, being essential for maintaining the glomerular filtration barrier (Turner et al., 2016). Previous work by the group of Vegt et al has shown that fragments of

**TABLE 1** | Cell binding of  $\text{Fe}_3\text{O}_4$ -DMSA-SMCC-BCZM- $^{99m}\text{Tc}$  and  $\text{Fe}_3\text{O}_4$ -DMSA- $^{99m}\text{Tc}$  in M165 cells without (w/o) and with blockage by unlabeled BCZM, at 24 h (% of Total Activity  $\pm$  SD,  $n = 3$ ).

Nanoradiopharmaceutical	Cell Uptake w/o block (%)	Cell uptake with block (%)
$\text{Fe}_3\text{O}_4$ -DMSA-SMCC-BCZM- $^{99m}\text{Tc}$	$25.27 \pm 1.84$	$10.74 \pm 0.88$
$\text{Fe}_3\text{O}_4$ -DMSA- $^{99m}\text{Tc}$	$5.88 \pm 1.06$	$5.07 \pm 1.29$



albumin might be suitable for inhibiting tubular reabsorption of peptides, however the effect of pre-administration of these agents on kidney uptake has not been investigated in the present study (Vegt et al., 2008). Lung uptake was high for both species at all time-points examined but it was significantly higher for the non-targeted species ( $64.51 \pm 8.44\% \text{ID/g}$  at 2 h p.i.), remaining quite high even at 24 h p.i. ( $28.27 \pm 1.45\% \text{ID/g}$ ). This may be attributed to various factors, such as the size of the nanoconstructs, their DMSA coating and, for the  $\text{Fe}_3\text{O}_4$ -DMSA-SMCC-BCZM- $^{99\text{m}}\text{Tc}$  species, its functionalization with BCZM (Chaves et al., 2002, 2005; Monge-Fuentes et al., 2011).

In the case of  $\text{Fe}_3\text{O}_4$ -DMSA-SMCC-BCZM- $^{99\text{m}}\text{Tc}$ , tumor accumulation was quick, starting at  $8.9 \pm 1.88\% \text{ID/g}$  at 2 h p.i., showed a slight increase at 4 h p.i. ( $16.21 \pm 2.56\% \text{ID/g}$ ) and then decreased at 24 h p.i. ( $6.01 \pm 1.69\% \text{ID/g}$ ). At all time-points studied, tumor uptake was significantly different ( $P < 0.05$ ) between the two radiolabeled species, in favor of the BCZM-functionalized MPNs. Even though there is a decrease in tumor uptake in time, the tumor-to-blood ratio reached a maximum at 24 h p.i. ( $\sim 7$ ), which is also the case for the tumor-to-muscle ratio ( $\sim 18$ ) (Figure 6D). A further interesting observation is that the non-targeted  $\text{Fe}_3\text{O}_4$ -DMSA- $^{99\text{m}}\text{Tc}$  showed practically no decline in tumor uptake value from 4 to 24 h p.i., which leads us to the conclusion that the nanoparticle shell

was stably labeled with  $^{99\text{m}}\text{Tc}$ , without being the subject of any degradation (Rainone et al., 2004). The decline in tumor uptake witnessed for  $\text{Fe}_3\text{O}_4$ -DMSA-SMCC-BCZM- $^{99\text{m}}\text{Tc}$  may be attributed to *in vivo* clearance of the nanoconstruct, however even if this is the case, there is significant increase in the tumor/blood ratio from 4 to 24 h p.i. Because of the high tumor contrast exhibited after functionalization of these IONPs with BCZM, showing us favorable tumor-to-background ratios, we expect to witness satisfactory imaging properties for this nanoconstruct. All other organs studied showed low or negligible uptake. The results clearly indicate that biomarker-mediated active targeting provided the best efficiency in breast-cancer-induced angiogenesis detection, compared to simple EPR passive accumulation.

Binding specificity of  $\text{Fe}_3\text{O}_4$ -DMSA-SMCC-BCZM- $^{99\text{m}}\text{Tc}$  was investigated by performing blocking experiments in M165 tumor-bearing mice at 4h post-injection of the radiotracer, after pre-injection of the mice with a large excess (2.5 mg) unlabeled BCZM. Tumor uptake was significantly different ( $P < 0.05$ ) between the blocked and unblocked mice ( $\sim 75\%$  accumulation decrease in the M165 tumor), thus confirming the binding specificity of  $\text{Fe}_3\text{O}_4$ -DMSA-SMCC-BCZM- $^{99\text{m}}\text{Tc}$  (Figure S6, Table S3). A significant decrease in kidney uptake was also demonstrated, indicating renal VEGF-A blocking.

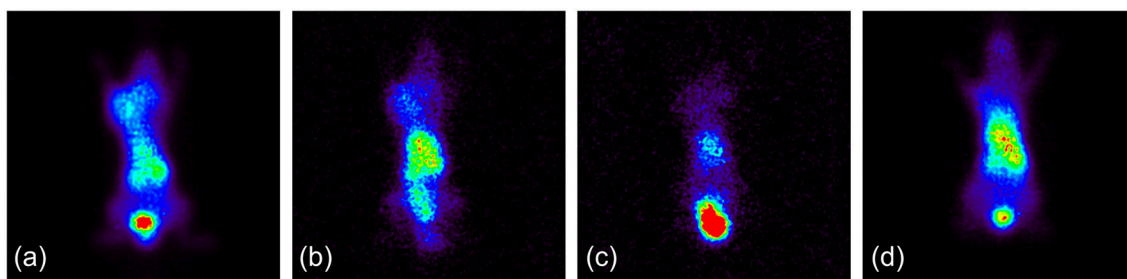


**FIGURE 7** | (a)  $\text{Fe}_3\text{O}_4$ -DMSA-SMCC-BCZM- $^{99\text{m}}\text{Tc}$ , imaging at 1 h p.i.; (b)  $\text{Fe}_3\text{O}_4$ -DMSA-SMCC-BCZM- $^{99\text{m}}\text{Tc}$ , imaging at 24 h p.i.; (c)  $\text{Fe}_3\text{O}_4$ -DMSA-SMCC-BCZM- $^{99\text{m}}\text{Tc}$ , blocking with excess BCZM 24 h prior to  $\text{Fe}_3\text{O}_4$ -DMSA-SMCC-BCZM- $^{99\text{m}}\text{Tc}$  administration, imaging at 1 h p.i.; (d)  $\text{Fe}_3\text{O}_4$ -DMSA- $^{99\text{m}}\text{Tc}$ , imaging at 1 h p.i.

### In Vivo Imaging Studies (Pilot Studies)

After evidence of tumor accumulation was provided by the *ex vivo* biodistribution study, and in order to evaluate the potential of VEGF-targeting IONPs as a dual-modality imaging agent, initial gamma-ray and MR imaging were performed on M165 tumor-bearing SCID mice to verify our hypothesis. Static planar scintigraphic images of a mouse injected with  $\text{Fe}_3\text{O}_4$ -DMSA-SMCC-BCZM- $^{99\text{m}}\text{Tc}$  at 1 h and 24 h post injection are shown in **Figures 7a,b**. These pilot images show significant accumulation of the radiotracer in the tumor from the first hour p.i., which was retained at the tumor site up to 24 h p.i. However, after administration of an excess of BCZM 24 h prior to injection of  $\text{Fe}_3\text{O}_4$ -DMSA-SMCC-BCZM- $^{99\text{m}}\text{Tc}$  (blocking study), no tumor uptake was present 1 h p.i. (**Figure 7c**). Furthermore, when the animal was injected with  $\text{Fe}_3\text{O}_4$ -DMSA- $^{99\text{m}}\text{Tc}$  (non-targeted nanoconstruct), practically no tumor uptake was seen (**Figure 7d**), as expected.

In the MR imaging experiment which was conducted, T2 weighted images acquired before administration of nanoparticles showed the tumors with high signal intensity. (**Figures 8a–c**). After nanoparticle administration the following day, decreased tumor MR signal intensity was noted, indicating specific uptake of  $\text{Fe}_3\text{O}_4$ -DMSA-SMCC-BCZM (**Figure 8d**), while the non-targeted nanoconstruct  $\text{Fe}_3\text{O}_4$ -DMSA showed only a slight drop in signal intensity (**Figure 8**). M165 tumor-bearing mice which were not injected with nanoparticles served as our control mice, and exhibited no drop in tumor signal intensity (**Figure 8**).

One of the most significant advantages of SPECT is its sensitivity, which is the reason why SPECT imaging tracers injected at very low concentrations are sufficient to provide high-quality images. However, this approach would prove to be problematic in the case of a dual-modality SPECT/MR imaging agent, since MR imaging requires much higher concentrations of injected contrast agent, in order to provide satisfactory images. Our MRI studies showed that a low-concentration nanomaterial injection ( $89\mu\text{g}/100\mu\text{l}/\text{mouse}$ , i.e., the injected dose of radiotracer for the gamma camera imaging) could not provide adequate contrast, while a high-concentration sample ( $1,000\mu\text{g}/100\mu\text{l}/\text{mouse}$ , **Figure 8**) was sufficient for contrast.

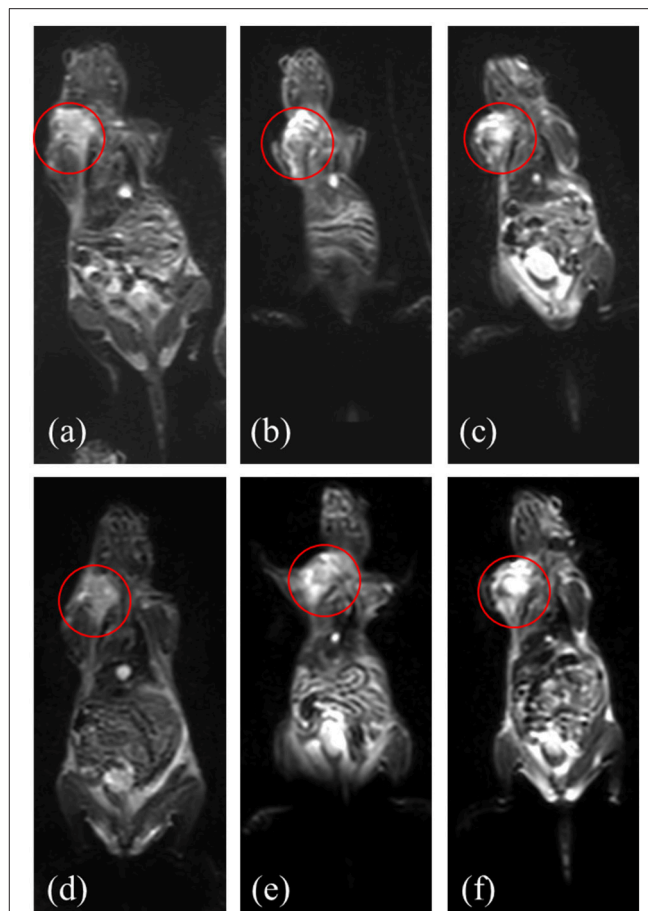
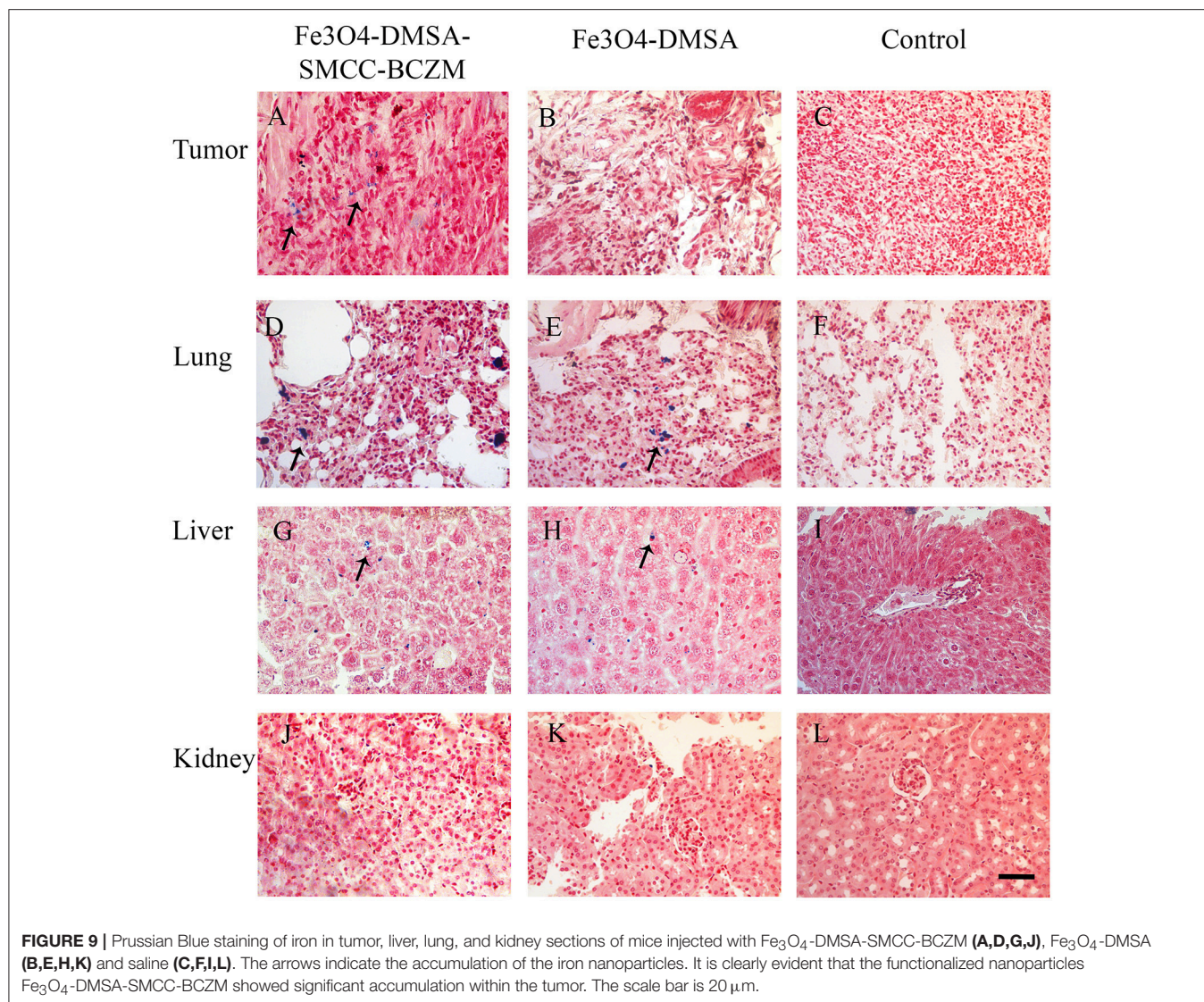


**FIGURE 8** | MR imaging of mice injected with  $\text{Fe}_3\text{O}_4$ -DMSA-SMCC-BCZM (**d**),  $\text{Fe}_3\text{O}_4$ -DMSA (**e**) and without injection of nanoparticles (**f**, control mice) at 4 h p.i.; images of the mice 1 day before nanoparticle injection (**a–c**, respectively). Red circles designate the tumor area.

For future applications, we will opt to work with nanoparticle samples having an adequately high concentration for satisfactory MR imaging, and to adjust the amount of radioisotope to provide an imaging tracer for simultaneous SPECT/MR imaging.



## Histopathology

Prussian blue staining of resected tumors from mice injected intravenously with non-functionalized Fe<sub>3</sub>O<sub>4</sub>-DMSA demonstrated little iron accumulation (**Figure 9B**), while Fe<sub>3</sub>O<sub>4</sub>-DMSA-SMCC-BCZM showed significant accumulation of iron within the tumor, suggesting improved tumor targeting for the antibody-functionalized nanoparticles (**Figure 9A**). Iron uptake was strong in the lungs of mice injected with both nanoconstructs (**Figures 9D,E**), while liver (**Figures 9G,H**) and kidneys (**Figures 9J,K**) also showed similar nanoparticle accumulation. Staining of tissues from mice injected with saline (control mice) showed no evidence of nanoparticle accumulation (**Figures 9C,E,I,L**). These findings are in line with our *ex vivo* and *in vivo* studies, and provide further proof of the targeting capabilities of Fe<sub>3</sub>O<sub>4</sub>-DMSA-SMCC-BCZM.

By performing this study, our intention was to show that the antibody-functionalized Fe<sub>3</sub>O<sub>4</sub>-DMSA-SMCC-BCZM exhibited targeted delivery to M165 tumors, while the non-functionalized

nanoconstruct Fe<sub>3</sub>O<sub>4</sub>-DMSA did not. We believe that both our *ex vivo* and *in vivo imaging* experiments, as well as the performed histopathology study, have proven the concept of our hypothesis.

## CONCLUSIONS

In this proof-of-concept study, we have successfully prepared and tested a dual-modality nanoplatform functionalized with the monoclonal antibody BCZM. We have demonstrated that our nanoconstruct does not cause toxic effects in normal and cancer cells and has the ability to bind to the VEGF-165 isoform overexpressed on M165 tumor cells, when labeled with <sup>99m</sup>Tc, forming stable constructs. *Ex vivo* biodistribution studies showed that the tumor-to-blood and the tumor-to-muscle ratios reached a maximum at 24 h p.i. (~7 and ~18 respectively), confirming high specificity of the antibody-functionalized tracer toward the overexpressed VEGF-165 isoform. Initial pilot *in vivo* images were in line with the *ex vivo* results, which were further proven

by the histopathology study. The overall encouraging preliminary results we have obtained warrant further investigation into the dual-modality capabilities of the developed probes. However, further modifications may be required to improve the *in vivo* behavior of these nanoconstructs.

The primary idea behind the design and synthesis of these NPs was to provide a platform for the development of a dual-modality molecular imaging agent. We envision that once the targeted nanoconstruct is efficiently delivered to its target, it can be developed into a therapeutic tool, by exploiting its magnetic properties after application of an external magnetic field to heat tissue or activate drug release. The theranostic potential of these NPs could be further enhanced after radiolabeling with Rhenium-188 ( $^{188}\text{Re}$ ), a therapeutic isotope with chemical properties similar to  $^{99\text{m}}\text{Tc}$ .

## AUTHOR CONTRIBUTIONS

CT, DS, and PB designed the study and analyzed the data. All authors contributed to the experimental execution of

the study, and to the writing process of the manuscript. All authors have read and approved of the final version of the manuscript.

## ACKNOWLEDGMENTS

The authors would like to thank Dr. Zili Sideratou (NCSR Demokritos, Institute of Nanoscience and Nanotechnology) for her support and assistance with DLS measurements. The authors would also like to acknowledge Mr. Stavros Xanthopoulos for excellent technical assistance, and Dr. Theodoros Tsotakos for valuable discussions. Finally, the authors kindly thank Dr. N. Kalogeropoulos, Dr. D. Stellas and Ms. E. Salvanou for assistance with the histopathology study.

## SUPPLEMENTARY MATERIAL

The Supplementary Material for this article can be found online at: <https://www.frontiersin.org/articles/10.3389/fchem.2018.00224/full#supplementary-material>

## REFERENCES

- Ai, F., Ferreira, C. A., Chen, F., and Cai, W. (2016). Engineering of radiolabeled iron oxide nanoparticles for dual-modality imaging. *Wiley Interdiscip. Rev. Nanomed. Nanobiotechnol.* 8, 619–630. doi: 10.1002/wnan.1386
- Anselmo, A. C., and Mitragotri, S. (2016). Nanoparticles in the clinic. *Bioeng. Transl. Med.* 1, 10–29. doi: 10.1002/btm2.10003
- Auffan, M., Decome, L., Rose, J., Orsiere, T., De Meo, M., Briois, V., et al. (2006). *In vitro* interactions between DMSA-coated maghemite nanoparticles and human fibroblasts: a physicochemical and cyto-genotoxic study. *Environ. Sci. Technol.* 40, 4367–4373. doi: 10.1021/es060691k
- Barrow, M., Taylor, A., Murray, P., Rosseinsky, M. J., and Adams, D. J. (2015). Design considerations for the synthesis of polymer coated iron oxide nanoparticles for stem cell labelling and tracking using MRI. *Chem. Soc. Rev.* 44, 6733–6748. doi: 10.1039/C5CS00331H
- Bertrand, N., Wu, J., Xu, X. Y., Kamaly, N., and Farokhzad, O. C. (2014). Cancer nanotechnology: the impact of passive and active targeting in the era of modern cancer biology. *Adv. Drug Deliver. Rev.* 66, 2–25. doi: 10.1016/j.addr.2013.11.009
- Bouziotis, P., Psimadas, D., Tsotakos, T., Stamopoulos, D., and Tsoukalas, C. (2013). Radiolabeled iron oxide nanoparticles as dual-modality SPECT/MRI and PET/MRI agents. *Curr. Top. Med. Chem.* 12, 2694–2702. doi: 10.2174/1568026611212230007
- Carmeliet, P. (2005). Angiogenesis in life, disease and medicine. *Nature* 438, 932–936. doi: 10.1038/nature04478
- Chauhan, V. P., Stylianopoulos, T., Boucher, Y., and Jain, R. K. (2011). Delivery of molecular and nanoscale medicine to tumors: transport barriers and strategies. *Annu. Rev. Chem. Biomol. Eng.* 2, 281–298. doi: 10.1146/annurev-chembioeng-061010-114300
- Chauhan, V. P., Stylianopoulos, T., Martin, J. D., Popović, Z., Chen, O., Kamoun, W. S., et al. (2012). Normalization of tumour blood vessels improves the delivery of nanomedicines in a size-dependent manner. *Nat. Nanotechnol.* 7, 383–388. doi: 10.1038/nnano.2012.45
- Chaves, S. B., Lacava, L. M., Lacava, Z. G. M., Silva, O., Pelegrini, F., Buske, N., et al. (2002). Light microscopy and magnetic resonance characterization of a DMSA-coated magnetic fluid in mice. *IEEE Trans. Magn.* 38, 3231–3233. doi: 10.1109/TMAG.2002.802495
- Chaves, S. B., Silva, L. P., Lacava, Z. G. M., Morais, P. C., and Azevedo, R. B. (2005). Interleukin-1 and interleukin-6 production in mice's lungs induced by 2, 3 meso-dimercaptosuccinic-coated magnetic nanoparticles. *J. Appl. Phys.* 97:10Q915. doi: 10.1063/1.1854531
- Chen, Y. C., Furenlid, L. R., Wilson, D. W., and Barrett, H. H. (2005). "Calibration of Scintillation Cameras and Pinhole SPECT Imaging Systems," in *Small-Animal SPECT Imaging*, eds M. A. Kupinski and H. H. Barrett (New York, NY: Springer), 195–201.
- Chen, Z. P., Zhang, Y., Zhang, S., Xia, J. G., Liu, J. W., Xu, K., et al. (2008). Preparation and characterization of water-soluble monodisperse magnetic iron oxide nanoparticles via surface double-exchange with DMSA. *Colloids Surf. A Physicochem. Eng. Asp.* 316, 210–216. doi: 10.1016/j.colsurfa.2007.09.017
- Costa, C., Brandão, F., Bessa, M. J., Costa, S., Valdiglesias, V., Kiliç, G., et al. (2016). *In vitro* cytotoxicity of superparamagnetic iron oxide nanoparticles on neuronal and glial cells. Evaluation of nanoparticle interference with viability tests. *J. Appl. Toxicol.* 36, 361–372. doi: 10.1002/jat.3213
- Cui, D., Lu, X., Yan, C., Liu, X., Hou, M., Xia, Q., et al. (2017). Gastrin-releasing peptide receptor-targeted gadolinium oxide-based multifunctional nanoparticles for dual magnetic resonance/fluorescence molecular imaging of prostate cancer. *Int. J. Nanomed.* 12, 6787–6797. doi: 10.2147/IJN.S139246
- de Souza Albernaz M, Toma, S. H., Clanton, J., Araki, K., and Santos-oliveira, R. (2018). Decorated superparamagnetic iron oxide nanoparticles with monoclonal antibody and diethylene-triamine-pentaacetic acid labeled with thechnetium-99m and gallium-68 for breast cancer imaging. *Pharm. Res.* 35:24. doi: 10.1007/s11095-017-2320-2
- De Rosales, R. T. M., Tavaré, R., Glaria, A., Varma, G., Protti, A., and Blower, P. J. (2011).  $^{99\text{m}}\text{Tc}$ -bisphosphonate-iron oxide nanoparticle conjugates for dual-modality biomedical imaging. *Bioconjug. Chem.* 22, 455–465. doi: 10.1021/bc100483k
- Eliceiri, B. P., and Cheres, D., A. (1999). The role of alphav integrins during angiogenesis: insights into potential mechanisms of action and clinical development. *J. Clin. Invest.* 103, 1227–1230. doi: 10.1172/JCI6869
- Fauconnier, N., Pons, J. N., Roger, J., and Bee, A. (1997). Thiolation of maghemite nanoparticles by dimercaptosuccinic acid. *J. Colloid Interface Sci.* 194, 427–433. doi: 10.1006/jcis.1997.5125
- Furenlid, L. R., Chen, Y. C., and Kim, H. (2005). "SPECT Imager Design and Data-Acquisition System," in *Small-Animal SPECT Imaging*, eds M. A. Kupinski and H. H. Barrett (New York, NY: Springer), 115–138.
- Furenlid, L. R., Wilson, D. W., Chen, Y. C., Kim, H., Pietraski, P. J., Crawford, M. J., et al. (2004). FastSPECT II: a second-generation high-resolution dynamic SPECT imager. *IEEE Trans. Nucl. Sci.* 51, 631–635. doi: 10.1109/TNS.2004.830975
- Galli, M., Guerrini, A., Cauteruccio, S., Thakare, P., Dova, D., Orsini, F., et al. (2017). Superparamagnetic iron oxide nanoparticles functionalized by peptide nucleic acids. *RSC Adv.* 7, 15500–15512. doi: 10.1039/C7RA00519A

- Hoffman, D., Sun, M., Yang, L., McDonagh, P. R., Corwin, F., Sundaresan, G., et al. (2014). Intrinsically radiolabeled [(59)Fe]-SPIONs for dual MRI/radiionuclide detection. *Am. J. Nucl. Med. Mol. Imaging* 4, 548–560.
- Hong, H., Yang, K., Zhang, Y., Engle, J. W., Feng, L., Yang, Y., et al. (2012). *In vivo* targeting and imaging of tumor vasculature with radiolabeled, antibody-conjugated nano-graphene. *ACS Nano* 6, 2361–2370. doi: 10.1021/nn204625e
- Jarockyte, G., Daugelaite, E., Stasys, M., Statkute, U., Poderys, V., Tseng, T. C., et al. (2016). Accumulation and toxicity of superparamagnetic iron oxide nanoparticles in cells and experimental animals. *Int. J. Mol. Sci.* 17:1193. doi: 10.3390/ijms17081193
- Karageorgou, M.-A., Vranješ-Djurić, S., Radović, M., Lyberopoulou, A., Antić, B., Rouchota, M., et al. (2017). Gallium-68 labeled iron oxide nanoparticles coated with 2, 3-dicarboxypropane-1,1-diphosphonic acid as a potential PET/MR imaging agent: a proof-of-concept study. *Contrast Media Mol. Imaging* 2017:6951240. doi: 10.1155/2017/6951240
- Karmani, L., Labar, D., Valembis, V., Bouchat, V., Nagaswaran, P. G., Bol, A., et al. (2013). Antibody-functionalized nanoparticles for imaging cancer: influence of conjugation to gold nanoparticles on the biodistribution of 89Zr-labeled cetuximab in mice. *Contrast Media Mol. Imaging* 8, 402–408. doi: 10.1002/cmmi.1539
- Lee, S., and Chen, X. (2009). Dual-modality probes for *in vivo* molecular imaging. *Mol. Imaging* 8, 87–100. doi: 10.2310/7290.2009.00013
- Lee, S. Y., Jeon, S. I., Jung, S., Chung, I. J., and Ahn, C.-H. (2014). Targeted multimodal imaging modalities. *Adv. Drug Deliv. Rev.* 76, 60–78. doi: 10.1016/j.addr.2014.07.009
- Lin, R., Huang, J., Wang, L., Li, Y., Lipowska, M., Wu, H., et al. (2018). Bevacizumab and near infrared probe conjugated iron oxide nanoparticles for vascular endothelial growth factor targeted MR and optical imaging. *Biomater. Sci.* doi: 10.1039/C8BM00225H
- Liu, S., Zhang, P., Ray Banerjee, S., Xu, J., Pomper, M. G., and Cui, H. (2015). Design and assembly of supramolecular dual-modality nanoprobes. *Nanoscale* 7, 9462–9466. doi: 10.1039/C5NR01518A
- Los, M., Roodhart, J. M., and Voest, E. E. (2007). Target practice: lessons from phase iii trials with bevacizumab and vatalanib in the treatment of advanced colorectal cancer. *Oncologist* 12, 443–450. doi: 10.1634/theoncologist.12-4-443
- Mejías, R., Gutiérrez, L., Salas, G., Pérez-Yagüe, S., Zotes, T. M., Lázaro, F. J., et al. (2013). Long term biotransformation and toxicity of dimercaptosuccinic acid-coated magnetic nanoparticles support their use in biomedical applications. *J. Control. Release* 171, 225–233. doi: 10.1016/j.jconrel.2013.07.019
- Mejías, R., Pérez-Yagüe, S., Roca, A. G., Pérez, N., Villanueva, A., Cañete, M., et al. (2010). Liver and brain imaging through dimercaptosuccinic acid-coated iron oxide nanoparticles. *Nanomedicine* 5, 397–408. doi: 10.2217/nnm.10.15
- Mendoza-Nava, H., Ferro-Flores, G., Ramírez, F. D. M., Ocampo-García, B., Santos-Cuevas, C., Aranda-Lara, L., et al. (2016). 177Lu-dendrimer conjugated to folate and bombesin with gold nanoparticles in the dendritic cavity: a potential theranostic radiopharmaceutical. *J. Nanomater.* 2016, 1–11. doi: 10.1155/2016/1039258
- Monge-Fuentes, V., Garcia, M. P., Henriques, M. C., Teixeira, D. S., Tomaz, C., and Azevedo, R. B. (2011). Biodistribution and biocompatibility of DMSA-stabilized maghemite magnetic nanoparticles in nonhuman primates. *Nanomedicine* 6, 1529–1544. doi: 10.2217/nnm.11.47
- Morales-Avila, E., Ferro-Flores, G., Ocampo-García, B. E., De Leon-Rodríguez, L. M., Santos-Cuevas, C. L., García-Becerra, R., et al. (2011). Multimeric system of Tc-99m-labeled gold nanoparticles conjugated to c[RGDFk(C)] for molecular imaging of tumor alpha(v)beta(3) expression. *Bioconjug. Chem.* 22, 913–922. doi: 10.1021/bc100551s
- Orocio-Rodríguez, E., Ferro-Flores, G., Santos-Cuevas, C. L., Ramírez, F., de, M., and Ocampo-García, B. E., Azorin-Vega, E., et al. (2015). Two novel nanosized radiolabeled analogues of somatostatin for neuroendocrine tumor imaging. *J. Nanosci. Nanotechnol.* 15, 4159–4169. doi: 10.1166/jnn.2015.9620
- Paik, S.-Y.-R., Kim, J.-S., Shin, S., and Ko, S. (2015). Characterization, quantification, and determination of the toxicity of iron oxide nanoparticles to the bone marrow cells. *Int. J. Mol. Sci.* 16, 22243–22257. doi: 10.3390/ijms160922243
- Pluen, A., Boucher, Y., Ramanujan, S., McKee, T. D., Gohongi, T., di Tomaso, E., et al. (2001). Role of tumor-host interactions in interstitial diffusion of macromolecules: cranial vs. subcutaneous tumors. *Proc. Natl. Acad. Sci. U.S.A.* 98, 4628–4633. doi: 10.1073/pnas.081626898
- Rainone, P., Riva, B., Belloli, S., Sudati, F., Ripamonti, M., Verderio, P., et al. (2004). Development of <sup>99m</sup>Tc-radiolabeled nanosilica for targeted detection of HER 2-positive breast cancer. *Int. J. Nanomed.* 12, 3447–3461. doi: 10.2147/IJN.S129720
- Ruiz, A., Morais, P. C., Bentes de Azevedo, R., Lacava, Z. G. M., Villanueva, A., and del Puerto Morales, M. (2014). Magnetic nanoparticles coated with dimercaptosuccinic acid: development, characterization, and application in biomedicine. *J. Nanoparticle Res.* 16:2589. doi: 10.1007/s11051-014-2589-6
- Ruiz, A., Salas, G., Calero, M., Hernández, Y., Villanueva, A., Herranz, F., et al. (2013). Short-chain PEG molecules strongly bound to magnetic nanoparticle for MRI long circulating agents. *Acta Biomater.* 9, 6421–6430. doi: 10.1016/j.actbio.2012.12.032
- Schroeder, A., Heller, D. A., Winslow, M. M., Dahlan, J. E., Pratt, G. W., Langer, R., et al. (2012). Treating metastatic cancer with nanotechnology. *Nat. Rev. Cancer* 12, 39–50. doi: 10.1038/nrc3180
- Shelat, R., Chandra, S., and Khanna, A. (2018). Detailed toxicity evaluation of beta-cyclodextrin coated iron oxide nanoparticles for biomedical applications. *Int. J. Biol. Macromol.* 110, 357–365. doi: 10.1016/j.ijbiomac.2017.09.067
- Shih, T., and Lindley, C. (2006). Bevacizumab: an angiogenesis inhibitor for the treatment of solid malignancies. *Clin. Ther.* 28, 1779–1802. doi: 10.1016/j.clinthera.2006.11.015
- Shukla, S., Jadaun, A., Arora, V., Sinha, R. K., Biyani, N., and Jain, V. K. (2015). *In vitro* toxicity assessment of chitosan oligosaccharide coated iron oxide nanoparticles. *Toxicol. Rep.* 2, 27–39. doi: 10.1016/j.toxrep.2014.11.002
- Stamopoulos, D., Benaki, D., Bouziotis, P., and Ziropiannis, P. N. (2007). *In vitro* utilization of ferromagnetic nanoparticles in hemodialysis therapy. *Nanotechnology* 18: 495102. doi: 10.1088/0957-4484/18/49/495102
- Torchilin, V. P. (2014). Multifunctional, stimuli-sensitive nanoparticulate systems for drug delivery. *Nat. Rev. Drug Discov.* 13, 813–827. doi: 10.1038/nrd4333
- Turner, R. J., Eikmans, M., Bajema, I. M., Bruijn, J. A., and Baelde, H. J. (2016). Stability and species specificity of renal VEGF-A Splicing patterns in kidney disease. *PLoS ONE* 11:e0162166. doi: 10.1371/journal.pone.0162166
- Varvarigou, A. D., Scopinaro, F., Leonidiadis, L., Corleto, V., and Schillaci, O., De Vincentis, G., et al. (2002). Synthesis, chemical, radiochemical and radiobiological evaluation of a new <sup>99m</sup>Tc-labelled bombesin-like peptide. *Cancer Biother. Radiopharm.* 17, 317–326. doi: 10.1089/10849780260179288
- van Vlerken, L. E., and Amiji, M. M. (2006). Multi-functional polymeric nanoparticles for tumour-targeted drug delivery. *Expert Opin. Drug Deliv.* 3, 205–216. doi: 10.1517/17425247.3.2.205
- Varvarigou, A. D., Archimandritis, S. C., Sekeri-Pataryas, K. E., Sourlingas, T. G., Sivolapenko, G., and Paschali, E. (1996). Radiochemical and radioimmunological data of <sup>99m</sup>Tc-anti-CEA labelled by two diverse methods. *Nucl. Med. Commun.* 17, 80–88. doi: 10.1097/00006231-199601000-00014
- Vegt, E., van Eerd, J. E., Eek, A., Oyen, W. J., Wetzels, J. F., de Jong, M., et al. (2008). Reducing renal uptake of radiolabeled peptides using albumin fragments. *J. Nucl. Med.* 49, 1506–1511. doi: 10.2967/jnumed.108.053249
- Wang, Y., Wang, Y., Wang, L., Che, Y., Li, Z., and Kong, D. (2011). Preparation and evaluation of magnetic nanoparticles for cell labeling. *J. Nanosci. Nanotechnol.* 11, 3749–3756. doi: 10.1166/jnn.2011.3822
- Zhong, Y., Meng, F., Deng, C., and Zhong, Z. (2014). Ligand-directed active tumor-targeting polymeric nanoparticles for cancer chemotherapy. *Biomacromolecules* 15, 1955–1969. doi: 10.1021/bm5003009

**Conflict of Interest Statement:** The authors declare that the research was conducted in the absence of any commercial or financial relationships that could be construed as a potential conflict of interest.

Copyright © 2018 Tsoukalas, Psimadas, Kastis, Koutoulidis, Harris, Paravatou-Petsotas, Karageorgou, Furenli, Mouloupoulos, Stamopoulos and Bouziotis. This is an open-access article distributed under the terms of the Creative Commons Attribution License (CC BY). The use, distribution or reproduction in other forums is permitted, provided the original author(s) and the copyright owner are credited and that the original publication in this journal is cited, in accordance with accepted academic practice. No use, distribution or reproduction is permitted which does not comply with these terms.